Hourly Biomass Burning Emissions Product from Blended Geostationary and Polar-orbiting Satellites for Air Quality Forecasting Applications

Fangjun Li[a*], Xiaoyang Zhang[a], Shobha Kondragunta[b], Xiaoman Lu[a], Ivan Csiszar[b], and Christopher C. Schmidt[c]

[a] Geospatial Sciences Center of Excellence, department of Geography and Geospatial Sciences, South Dakota State University, Brookings, SD 57007, USA

[b] NOAA/NESDIS/Center for Satellite Applications and Research, College Park, MD 20740, USA

[c] Cooperative Institute for Meteorological Satellite Studies (CIMSS), University of Wisconsin-Madison, Madison, WI 53706, USA

* Corresponding author: Fangjun Li (email: fangjun.li@sdstate.edu); Xiaoyang Zhang (email: xiaoyang.zhang@sdstate.edu); Shobha Kondragunta (shobha.kondragunta@noaa.gov)

Abstract

Biomass burning influences atmospheric composition and regional air quality. The hourly biomass-burning emissions are usually required by air quality models, yet most available emission inventories provide daily or monthly estimates in 0.1 degree or coarser grids, limiting the prediction accuracy. The Advanced Baseline Imager (ABI) on the Geostationary Operational Environmental Satellites – R Series (GOES-R) observes fires across the conterminous United States (CONUS) every 5 minutes at a spatial resolution of 2 km, which allows for characterizing fires and emissions on diurnal scale. In this study, we developed a new operational algorithm to generate regional hourly 3 km fire emission across the CONUS by fusing temporally resolved ABI fire radiative power (FRP) and fine spatial-resolution (375m) FRP from the Visible Infrared Imaging Radiometer Suite (VIIRS) on the Joint Polar Satellite System (JPSS) satellites. To do this, ABI FRP was first calibrated against and fused with VIIRS FRP in 3 km grids. Then, FRP diurnal cycles at an interval of 5 minutes were reconstructed using the fused ABI-VIIRS FRP and the land cover-ecoregion-specific FRP diurnal climatologies. The reconstructed FRP diurnal cycles were applied to estimate hourly emissions of eight species (e.g., carbon monoxide (CO) and fine particulate matter with diameters < 2.5 μm ($PM_{2.5}$)). The accuracy was verified by comparing with CO observations from the TROPOspheric Monitoring Instrument (TROPOMI) on the Sentinel-5 Precursor satellite, and with $PM_{2.5}$ emissions from eight other inventories. The results of the ABI-VIIRS estimates during one year from April 2020 to March 2021 indicate that fires burned 221 Tg dry matter and emit 2.25 Tg $PM_{2.5}$ emissions across the CONUS. The seasonal and diurnal patterns of emissions vary with land cover types. The largest and smallest seasonal variations are shown in forest and agriculture fire emissions, respectively. The diurnal emission patterns of different land cover types share similar shapes but differ largely in

magnitude. Moreover, the diurnal pattern of forest fire emissions suggests that emissions are dominated during daytime in the eastern U.S. but strong during both daytime and nighttime in the western U.S. The evaluation shows that the fused ABI-VIIRS based CO agrees well with the TROPOMI CO, with a difference of 11%. However, the agreement between fused ABI-VIIRS emissions and other inventories varies for different fire events.

Keywords: GOES-R ABI, JPSS VIIRS, Sentinel-5P TROPOMI, FRP, fusion, fire emission

1. Introduction

Trace gases including greenhouse gases and aerosol emissions emitted from open biomass burning influence climate, global carbon cycle, and public health profoundly (Friedlingstein et al., 2020; IPCC, 2021; Johnston et al., 2012). Global fires emit 2.2 Pg carbon emissions and 36 Tg fine particulate matter (mass of PM in $\mu g/m^3$ for particles with a diameter less than 2.5μm, or $PM_{2.5}$) into the atmosphere annually (van der Werf et al., 2017; van Marle et al., 2017). The annual carbon emissions from fires have been as much as 23% and 138% of annual carbon emissions from fossil fuels and land-use change, respectively, in the past two decades (Friedlingstein et al., 2020). Carbon dioxide (CO_2) emissions from deforestation fires play an important role in the inter-annual variability of the atmospheric GHG budgets (IPCC, 2021). Smoke aerosols scatter and absorb incoming solar radiation and inhibit cloud formation, resulting in a net radiative forcing of +0.20 - +0.52 W m^{-2} (Bond et al., 2013; Jacobson, 2014; Kaufman et al., 2005). Furthermore, smoke aerosols cause public health and transportation issues by degrading regional air quality and visibility (Ford et al., 2018; Jaffe et al., 2020; Johnston et al., 2012; Li et al., 2021b). Therefore, fire emissions are considered an essential input for climate and air quality forecast models, and accurate estimation of fire emissions is critical to understand the roles of biomass burning (Appel et al., 2017; Inness et al., 2019; Reid et al., 2009; Wang et al., 2018, Brown et al., 2021; Carter et al., 2020; Ye et al., 2021).

Three types of methods have been developed for emissions estimation. First, fire emissions have been conventionally calculated using four parameters: total area burned (BA), fuel loadings (FL), combustion completeness (CC), and emission factors (EF) since the 1980s (Seiler and Crutzen, 1980). Before the 2000s, regional and global emission estimates were highly uncertain due to the lack of consistent fire data at large scales and very simplified assumptions of

each parameter (Crutzen and Andreae, 1990; Hao et al., 1990; Seiler and Crutzen, 1980). Since 2000, the availability of burned area and active fire products from the Moderate Resolution Imaging Spectroradiometer (MODIS) on NASA's Terra and Aqua satellites enabled the computation of consistent emissions estimates at large scales (van der Werf et al, 2006). The associated global inventories include the Fire Locating and Modeling of Burning Emissions (FLAMBE) (Reid et al., 2009), the Global Fire Emission Database (GFED) (van der Werf et al., 2017), and the Fire INventory from NCAR (FINN) (Wiedinmyer et al., 2011). The regional inventories include the Wildland Fire Emissions Information System (WFEIS) for North America (French et al., 2014), Brazilian Biomass Burning Emissions Model (3BEM) for South America (Archer-Nicholls et al., 2015), and the Missoula Fire Lab Emission Inventory (MFLEI) for the Conterminous United States (CONUS) (Urbanski et al., 2018). However, the widely used MODIS burned area products tend to miss a considerable number of small burns in fire-prone African Savanna (Roteta et al., 2019; Roy et al., 2019), deforestation fires in partially cloudy Tropical Forests (Boschetti et al., 2019; Liu et al., 2020; Vetrita et al., 2021), surface fires in Temperate Forests (Huang et al., 2018; Nowell et al., 2018), and agriculture burns (Liu et al., 2019; Randerson et al., 2012) that has been highlighted by Chuvieco et al. (2020). These missed burned areas lead to large uncertainties in emission estimates, which has been demonstrated recently in Africa (Ramo et al., 2021). Furthermore, the other parameters in the conventional approach also contain considerable uncertainties. Fuel loadings are calculated commonly based on either modeled carbon fluxes or static values summarized from literatures or static fuel maps at coarse resolutions (French et al., 2011; van der Werf et al., 2017; Wiedinmyer et al., 2011). These calculations likely cause large uncertainties due to misclassification of vegetation at coarse resolutions, large variability of fuel characteristics at fine scales, seasonal and inter-annual fuel

dynamics, and the imprecision of satellite-based estimates of surface and ground fuel loadings and characteristics (Di Giuseppe et al., 2021; French et al., 2011; Keane, 2013; Ottmar, 2014; Prichard et al., 2019; van Wees and van der Werf, 2019; Weise and Wright, 2014; Zhang et al., 2008). Further, it is difficult to obtain combustion completeness accurately at large scales because it varies with fuel type, size, shape, and moisture content and burn severity (Campbell et al., 2007; French et al., 2011; Hély et al., 2003; Veraverbeke and Hook, 2013). As a result, global conventional inventories usually use a fixed combustion completeness value for a given fuel stratum (e.g., GFED) or tree cover group (e.g., FINN) across different biomes (van der Werf et al., 2017; Wiedinmyer et al., 2011). Finally, emission factor is often compiled from global lab-, ground-, and airborne-based studies (Akagi et al., 2011; Andreae, 2019; Prichard et al., 2020; Urbanski, 2014; Yokelson et al., 2013). However, it is known to vary significantly with fire types, chemical properties of fuels, and combustion phases (Liu et al., 2017; Liu et al., 2016; Parker et al., 2016; Urbanski, 2014). Integrating the four parameters in emissions estimation, the associated uncertainties could result in exponential overestimation or underestimation due to compounding and compensating errors.

Second, inverse modeling methods have been also applied to estimate regional and global fire emissions with satellite observations (e.g., nitrogen oxides (NO_x) and carbon monoxide (CO)) (Streets et al., 2013). These methods, conventionally applied to anthropogenic sources and referred to as top-down methods, are often conducted using chemical transport models (CTMs) (Streets et al., 2013). However, the emissions estimates from different studies show large differences (Duncan et al., 2007; Jiang et al., 2017; Konovalov et al., 2014; Kopacz et al., 2010; Shindell et al., 2006; van der Velde et al., 2021). Their accuracy could be affected by several factors, including, but not limited to, uncertainties in physical, chemical, and meteorological

variables involved in inverse modeling and CTMs, aggregation errors of emissions sources, errors in transport and chemistry, and quality of satellite observations (Duncan et al., 2007; Jiang et al., 2011; Shindell et al., 2006; Streets et al., 2013). These factors can influence the accuracy of emissions by >20% globally and >80% regionally (Jiang et al., 2011 & 2013).

Third, satellite fire radiative power (FRP) provides an alternative pathway to the estimation of biomass-burning emissions. FRP, the instantaneous fire radiative energy, is linked to the rates of biomass combustion and fire emissions via a biomass combustion coefficient and smoke coefficient, respectively (Kaufman et al., 1998; Wooster, 2002). Their empirical relationships have been further proven in lab and field experiments (Freeborn et al., 2008; Ichoku et al., 2008; Kremens et al., 2012), and landscape wildfires in several fire-prone regions, including Africa (Mota and Wooster, 2018; Nguyen and Wooster, 2020; Roberts et al., 2005), South America (Pereira et al., 2009), boreal Russia (Konovalov et al., 2014), Indonesia (Lu et al., 2019; Lu et al., 2021) and United States (Li et al., 2020b; Li et al., 2018b; McCarley et al., 2020; Wiggins et al., 2020), as well as across the globe (Ichoku and Ellison, 2014; Jin et al., 2021; Vermote et al., 2009). The development and advancement of the empirical relationships have also been summarized in detail by a recent review (Wooster et al., 2021). Therefore, satellite FRP retrievals have been commonly applied to estimate biomass-burning emissions (Kumar et al., 2011; Li et al., 2021a; Li et al., 2019; Liu et al., 2015; Roberts et al., 2009; Vermote et al., 2009; Wooster et al., 2018; Zhang et al., 2020; Zheng et al., 2021). The emissions inventories include global biomass burning emission product from geostationary satellites (Zhang et al., 2012); Blended Global Biomass Burning Emissions (GBBEPx3.0, Zhang et al., 2019), Quick Fire Emissions Dataset (QFED2.5, Darmenov et al., 2015), Fire Energetics and Emissions

Research (FEER1.0, (Ichoku & Ellison, 2014)), and Global Fire Assimilation System (GFAS1.2, Kaiser et al., 2012).

Compared with the conventional burned-area based approach, the FRP-based method is superior in two aspects. First, it bypasses uncertainties in three parameters (BA, FL, and CC), thereby improving emissions estimation potentially. Second, it computes emissions at much higher temporal resolutions (i.e., daily or hourly), which is critical to time-sensitive applications. For instance, air quality forecast models usually require hourly emissions. Because diurnal emissions are not provided in the available inventories, models assume the same emissions rate during the day or redistribute daily emissions to a fixed diurnal climatology, which results in large uncertainties in model predictions (Bela et al., 2022; O'Neill et al., 2021; Ye et al., 2021).

The accuracy of FRP-based emissions estimation relies largely on the quality of FRP diurnal cycles that are indispensable for computing total fire radiative energy (FRE) and mass of emissions. Sensors on polar orbiting satellites (e.g., MODIS and the Visible Infrared Imaging Radiometer Suite (VIIRS)) can observe relatively small and cool fires due to their higher spatial resolutions than geostationary sensors (Csiszar et al., 2014; Giglio et al., 2016; Schroeder et al., 2014). Nevertheless, each sensor only provides fire observations twice a day in clear-sky condition or none due to obscuration of clouds, which are too temporally sparse to depict FRP diurnal cycles. Regardless of this fact, most FRP-based emissions inventories (i.e., QFED2.5, GFAS1.2, FEER1.0, and GBBEPx3.0) compute FRE and emissions using FRP from MODIS and/or VIIRS by simply assuming that very limited daily FRP observations can still be used to derive emissions. This assumption results in overestimated FRE and emissions when nocturnal fire activity is limited (Andela et al., 2015; Li et al., 2021a) but underestimated estimates when daytime FRP peaks at hours other than MODIS or VIIRS overpass times (Andela et al., 2015).

Although FRP diurnal cycles were reconstructed by superimposing predefined Gaussian-shaped curves to MODIS FRP (Andela et al., 2015; Vermote et al., 2009), the peak hour and fire duration were shown to be misrepresented (Andela et al., 2015; Li et al., 2019; Saide et al., 2015; Ye et al., 2021).

Geostationary satellites observe fires at high temporal resolution (i.e., every 5-15 minutes), which enables the reconstruction of FRP diurnal cycles, yet they tend to miss small and/or cool fires due to their coarser spatial resolution, especially at large view angles (Roberts and Wooster, 2008; Schmidt et al., 2012; Xu et al., 2021a; Xu et al., 2017). To improve the generation of FRP diurnal cycles and the calculation of FRE, it has been demonstrated that fusing FRP from fine spatial-resolution polar orbiting and high temporal-resolution geostationary satellites is promising (Freeborn et al., 2009; Li et al., 2021a; Li et al., 2019; Zhang et al., 2020). The potential of this approach is elevated greatly with the launches of the new-generation sensors, such as the Advanced Baseline Imager (ABI) on the Geostationary Operational Environmental Satellite R Series (GOES-R and the VIIRS sensor onboard Suomi NPP (Suomi National Polar orbiting Partnership) and JPSS (Joint Polar Satellite System) series. The ABI observes fires in 2 km pixels at nadir, with an unprecedented temporal resolution of 5 minutes across the CONUS and 10 minutes over North and South Americas (Schmit et al., 2017), and VIIRS provides FRP for daily global fires at the finest spatial resolution of 375 m (Schroeder et al., 2014). Similarly, the Advanced Himawari Imager (AHI) on Himawari-8/9 provides high-temporal-resolution fire observations in Asia (Bessho et al., 2016) and the Flexible Combined Imager (FCI) on the planned Meteosat Third Generation (MTG) will also provide high-temporal-resolution fire observations in Africa and Europe (Holmlund et al., 2021). The new fire data from Sentinel-3 will expand the long-term MODIS fire data at late morning (Xu et al., 2021b).

In this study, we develop a new algorithm that computes hourly biomass-burning emissions product at a spatial resolution of 3 km across the CONUS by fusing ABI and VIIRS FRP. This product named hourly Regional ABI and VIIRS fire Emissions (RAVE) produces fire emissions to air quality forecast model applications, including NOAA operational models such as the High Resolution Rapid Refresh smoke model (HRRR-smoke), Community Multiscale Air Quality (CMAQ) model, and Weather and Research Forecasting model coupled with Chemistry (WRF-Chem). These models operate currently at varying degrees of grid resolution and projections, with eventually all models migrating to 3-km spatial resolution. To facilitate the use of RAVE emissions product by multiple models, we decided to generate the product in a regular latitude-longitude grid with 0.03° resolution (simply called 3km grid in the following text). In doing so, any model can project the emissions onto its horizontal resolution. This paper describes the new algorithm of emissions estimation using ABI and VIIRS FRP and then investigates the accuracy of the RAVE product.

2. Data

2.1. VIIRS active fire data

VIIRS onboard the sun-synchronous Suomi NPP and NOAA-20 satellites crosses the equator at 1:30 AM and 1:30 PM local time, but NOAA-20 VIIRS observes the same location approximately 50 minutes before or after Suomi NPP due to the half-orbit separation of the two satellites (Wolfe et al., 2013). VIIRS has a wide swath of 3000 km along the scan direction, which enables the instrument to observe the entire globe without gaps (Cao et al., 2014). VIIRS is equipped with a dedicated moderate resolution 4-μm band for fire monitoring (M13, 750 m) with a high saturation level to allow for FRP retrievals for the vast majority of fire pixels.

Additionally, the imaging resolution (375m) I4 band provides better detection sensitivity and spatial detail, but limited potential for FRP retrievals due to its lower saturation. This band configuration led to the development of two active fire products: an M-band only heritage product (Csiszar et al. 2014), and an improved I-band / M-band hybrid product (Schroeder et al., 2014; hereafter referred to as the I-band product). Due to the onboard pixel aggregation and bow-tie deletion, VIIRS pixel size is generally more consistent across different scan angles from nadir to the scan edge and overlaps between consecutive scan lines are sharply reduced in comparison with MODIS (Cao et al., 2014). This leads to relatively consistent fire detection capability in the full range of scan angles and negligible repeating detections of the same fire between scan lines (Li et al., 2020a; Li et al., 2018a). Because the VIIRS I-band can observe many more small fires (i.e., FRP $\geq$ 4 MW) relative to VIIRS M-band and MODIS (Fu et al., 2020; Li et al., 2020a, 2021a; Li et al., 2020c; Schroeder et al., 2014), we used the 375m VIIRS I-band active fire product in this study.

We obtained NOAA operational Suomi NPP and NOAA-20 VIIRS I-band Level 2 (L2) active fire products from NOAA's the Comprehensive Large Array-data Stewardship System (CLASS, https://www.class.noaa.gov/). Defined in sensing geometry (or granule), for each fire detection, the VIIRS I-band L2 fire product provides observation time and location, FRP, satellite view zenith angle (VZA), solar zenith angle (SZA), persistent anomaly flag, and brightness temperatures in the 3.7 μm and 11 μm bands (Schroeder et al., 2020). Because of a low saturation temperature (367 K), the VIIRS 3.7 μm I4 band is saturated frequently over intense fires, hindering FRP calculation (Schroeder et al., 2014). Therefore, FRP for an I-band fire pixel is computed using the mid-infrared method (Wooster et al., 2005) with the co-located radiance in the 4-μm M13 band with a high nominal saturation temperature (634 K) (Csiszar et

al., 2014; Schroeder et al., 2020). For the sake of simplicity, the 375m VIIRS I-band FRP is referred to as VIIRS FRP hereafter. The persistent anomaly flag in this product indicates that a fire pixel may correspond to a hot spot not associated with biomass burning, such as gas flares, volcanos, solar farms, urban, and other non-fire signals (Schroeder et al., 2020). Thus, these fire detections were excluded in this study. Furthermore, the VIIRS I-band L2 fire product also provides fire mask that classifies fire and non-fire (clear/cloudy) pixels.

For the correction of cloud impacts on FRP (c.f. Section 3.1), we also obtained Suomi NPP and NOAA-20 VIIRS I-band geolocation product (namely GITCO) from NOAA CLASS to locate cloud pixels from fire mask.

2.2. ABI active fire data

GOES-R ABI observes fires every 5 minutes across the CONUS and every 10 minutes over North and South Americas (full disk scan) in its current default operational mode, with a nominal pixel size of 2 km at nadir (Schmit et al., 2017). The first two GOES-R satellites - GOES-16 and GOES-17, positioned at 75°W and 137°W above the equator, have been running operationally since December 2017 and February 2019, respectively (Schmit et al., 2017). GOES-16 observes the CONUS from the east, with a VZA of 29° - 72°, while GOES-17 scans the CONUS from the west, with a VZA of 44° - 84°. The NOAA ABI active fire algorithm detects fires mainly using the 3.9 and 11.2 μm bands (Schmidt et al., 2012). For each fire detection, the ABI active fire product provides the observation location (coordinates) and time, FRP, fire flag, and the legacy instantaneous fire size and fire temperature estimates, which are not utilized in this study (Schmidt et al., 2012). FRP is calculated from the radiances in the 3.9 μm band and its accuracy for intense fires is improved because of the enhanced saturation

269 temperature (411 K) of the ABI 3.9 μm band relative to legacy GOES satellites (Schmidt et al.,
270 2012; Schmit et al., 2017). Fire detections are flagged into six groups: processed (good quality),
271 saturated, cloud/smoke partially contaminated, high-, medium-, and low-probability (Schmidt et
272 al., 2012). The first three categories indicate very confident detections that meet all algorithm
273 tests while the other three categories suggest potential detections that only pass some of the
274 algorithm tests. FRP is provided for all processed fires, most saturated, cloud contaminated, and
275 high- and medium- possibility fires, and some low possibility fires.

276 The ABI L2 active fire product is generated in the ABI fixed grid projection. The
277 projection defines the CONUS scan domain using 1500 by 2500 pixels. The product has been
278 validated using the 30 m Landsat-8 and 375 m VIIRS fire detections and ground fire records
279 across the southeast CONUS. The validation revealed that the ABI can observe low-intensity
280 fires with an FRP as small as 34.5 MW confidently and fires that are missed by VIIRS due to
281 obscuration of clouds or forest canopy (Li et al., 2020c). To make the best of ABI high temporal
282 resolution in the reconstruction of FRP diurnal cycles, we obtained the ABI Level 2 active fire
283 product for the 5-minute CONUS scan mode from NOAA CLASS. The data period for this
284 analysis was three years from 2018 to 2020 for GOES-16 and one year of 2020 for GOES-17.

285 To remove false alarms, we preprocessed ABI fire detections using two strategies. First,
286 because false alarms are mainly associated with fire detections masked as high, medium, and low
287 possibility (Li et al., 2020c), we only considered high/medium/low possibility fire pixels if these
288 pixels were also detected as processed and saturated fire detections at least once during a 24h
289 window. Second, we used two persistent anomaly masks (for both GOES-16 and GOES-17) to
290 remove false alarms related to gas flares, solar farms, urban, etc. The anomaly masks were based

on the persistent anomaly information used in the NOAA VIIRS active fire products (Schroeder et al., 2020).

We also downloaded the ABI Level-1b (L1b) radiance product in the 5-minute CONUS scan mode from NOAA CLASS. The reflectances of four ABI bands (0.47 μm, 0.64 μm, and 0.86 μm) were chosen to generate true-color images in determining fresh fire smoke plumes for the evaluation purpose (c.f. Section 3.4).

2.3. Land cover and ecoregion maps

We used land cover and ecoregion maps to classify fire detections and FRP for reconstructing FRP diurnal cycles. First, a 3 km land cover map was generated by aggregating vegetation classes from the 500 m MODIS land cover product in 2019 (Friedl et al., 2010). It consists of five main land cover types: (1) forest (including evergreen needleleaf and broadleaf, deciduous needleleaf and broadleaf, and mixed forests classes), (2) shrubland (including closed and open shrublands classes), (3) savannas (including savannas and woody savannas classes), (4) grassland (including grasslands and permanent wetlands classes), and (5) cropland (including croplands and cropland-natural vegetation mosaics classes). Second, a 3-km ecoregion map was generated from the Level I North America ecoregions developed by the United States Environmental Protection Agency (EPA, https://www.epa.gov/eco-research/ecoregions-north-america, last accessed on 12/01/2021). As a result, there are five main land cover types in 11 ecoregions (Figure 1).

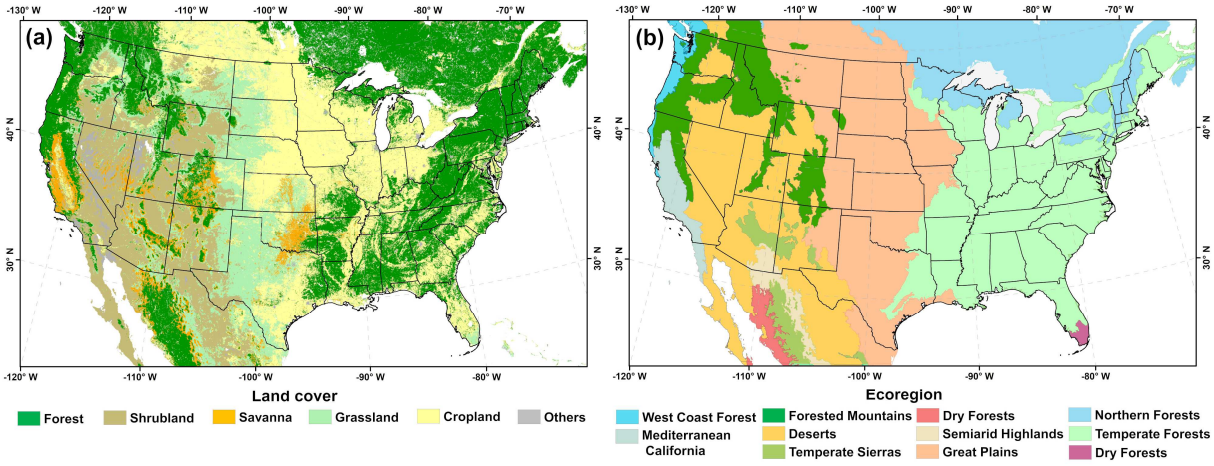

311

312 Figure 1. Land cover and ecoregion maps across the CONUS.

313

314 2.4. TROPOMI carbon monoxide (CO) data

315 We used TROPOMI L2 CO product to evaluate the RAVE CO emissions (c.f. Section
316 3.4). TROPOMI onboard the Copernicus Sentinel 5 Precursor satellite (Sentinel-5P) observes
317 key atmospheric species (e.g., CO, CO2, methane, NO_x, etc.) at approximately 1:35 PM local
318 time, merely 5 minutes later than the SNPP VIIRS afternoon overpass (Veefkind et al., 2012).
319 The daily TROPOMI CO is retrieved from radiance in the shortwave infrared band (SWIR,
320 2305–2385 nm) using the Shortwave Infrared CO Retrieval (SICOR) algorithm (Landgraf et al.,
321 2016; Vidot et al., 2012). For each pixel (5.5 km at nadir, enhanced from the previous 7 km in
322 late 2019), the L2 CO product provides observation time and location, VZA, SZA, and the total
323 column density of CO (mol m^{-2}). The product accuracy has been well demonstrated using total
324 column averaging kernels and ground-based CO (Borsdorff et al., 2018a, 2018b, and 2018c).
325 Borsdorff et al. (2018a) reveals that in clear-sky conditions, the vertical CO averaging kernels
326 are nearly 1.0 across the global, which indicates that the TROPIMI CO retrievals are close to the
327 true CO total column (Borsdorff et al., 2018a). Furthermore, the validations based on ground CO

suggest that the bias of the TROPOMI CO is very small (6 parts per billion (ppb)) (Borsdorff et al., 2018b and 2018c). We obtained the L2 CO product from the Copernicus open access hub (https://scihub.copernicus.eu/; last accessed on 12/01/2021) for the period of April 2020 – March 2021.

2.5. Other biomass-burning emissions inventories

We used six global emissions inventories (QFED2.5, GBBEPx4.0, FEER1.0, GFAS1.2, GFED4s, and FINN2.4) and two regional inventories (WFEIS v2.0 and fire emissions from California Air Resources Board or CARB) for comparing with emissions estimated in this study. The details are summarized in Table 1. Among eight inventories, QFED2.5, GBBEPx4.0, FEER1.0, and GFAS1.2 are based on the FRP approach. The QFED2.5 emissions are estimated from MODIS FRP via emissions coefficients, which are obtained initially by linking MODIS FRP to GFED3.1 fuel consumption and further tuned using MODIS aerosol optical depth (AOD) (Darmenov and Silva, 2015). GBBEPx3.0 estimates emissions using MODIS and 750m VIIRS FRP and emissions coefficients (Zhang et al., 2019). It has been upgraded recently to a new version GBBEPx4.0 that uses 375 m VIIRS I-band FRP and emissions coefficients, which are derived by relating 375m VIIRS FRP to historical QFED2.5 emissions. The FEER1.0 inventory estimates emissions in two steps. First, it computes the mass of total particular matter (TPM) from MODIS FRP via TPM emission coefficients, which are obtained using MODIS FRP and AOD observations over smoke plumes (Ichoku and Ellison, 2014). Second, the mass of other chemical species is estimated based on TPM mass and the ratio of the associated emission factors to TPM emission factor (Ichoku and Ellison, 2014). The GFASv1.2 emissions are

estimated using MODIS FRP and land cover specific biomass combustion coefficient (Kaiser et al., 2012).

GFED4s, FINN2.4, and two regional inventories are based on the conventional approach. For the GFED4s inventory, total area burned is from MODIS burned area product, and fuel loadings are modeled using a biochemical model (van der Werf et al., 2017). Note that for years from 2017 onward GFED4s estimates emissions using MODIS fire detections instead, which differs from the version before 2017. For the FINN2.4 inventory, total area burned is estimated from MODIS and VIIRS active fire observations, and fuel loadings are summarized from literatures (Wiedinmyer et al., 2011). The WFEIS2.0 estimates emissions across North America using MODIS burned area (Collection 6) and fuel loadings from the fuel characteristic classification system (FCCS) (French et al., 2014). CARB estimates fire emissions for California State using the FCCS fuel loadings and burned area reported by California Department of Forestry and Fire Protection (CAL FIRE) (CARB, 2021).

To compare multiple emissions inventories in individual fire events, we also used 30m Landsat Level-3 Burned Area (BA) data (Hawbaker et al., 2020) to delineate wildfires occurred in California during the record-breaking 2020 fire season. In the fire season, the largest August Complex Fire topped California's four-decade fire records since the 1980s and the other four largest fires were also among the historical ten largest wildfires (National Interagency Fire Center (NIFC), https://www.nifc.gov/fire-information/statistics, last accessed on 12/01/2021). The Landsat BA data were downloaded from the U.S. Geological Survey (USGS) EarthExplorer data port.

372 **Table 1.** Eight biomass-burning emissions inventories

Inventory	Resolution	Method	Input data	Reference & Data access
QFED2.5	global daily 0.25˚×0.3125˚ 0. 1˚×0.1˚,	FRP-based	MODIS FRP	Darmenov and Silva., 2015 https://portal.nccs.nasa.gov/datashare/iesa/aerosol/emissions/QFED/v2.5r1/
GBBEPx4.0	global daily 0.25˚×0.3125˚ 0.1˚×0.1˚, 25km	FRP-based	VIIRS FRP (375m)	Zhang et al., 2019 https://www.ospo.noaa.gov/Products/land/gbbepx/
FEER1.0	global daily 0.1˚×0.1˚,	FRP-based	MODIS FRP	Ichoku and Ellison., 2014 http://feer.gsfc.nasa.gov/data/emissions/
GFAS1.2	global daily 0.1˚×0.1˚	FRP-based	MODIS FRP	Kaiser et al., 2012 https://apps.ecmwf.int/datasets/data/cams-gfas/
GFED4s	global monthly 0.25˚×0.25˚,	burned area-based	MODIS burned area (C5), modeled fuel loadings	van der Werf et al., 2017 https://www.globalfiredata.org/
FINN2.4	global daily point	burned area-based	MODIS and 375m VIIRS fire detections, published fuel loadings	Wiedinmyer et al., 2011 http://bai.acom.ucar.edu/Data/fire/
WFEIS2.0	North America, monthly	burned area-based	MODIS burned area (C6) FCCS fuel loadings	French et al., 2014 https://wfis.mtri.org/
CARB	California State, annual	burned area-based	Agency-reported burned area, FCCS fuel loadings	https://ww2.arb.ca.gov/wildfire-emissions

373

374

375

3. Methods

The algorithm for hourly 3km emissions estimation proposed by this study is illustrated in Figure 2. The accuracy of the emission estimates was evaluated using the independent CO observations from S5P TROPOMI over selected fire events, and further compared with eight available biomass-burning emissions.

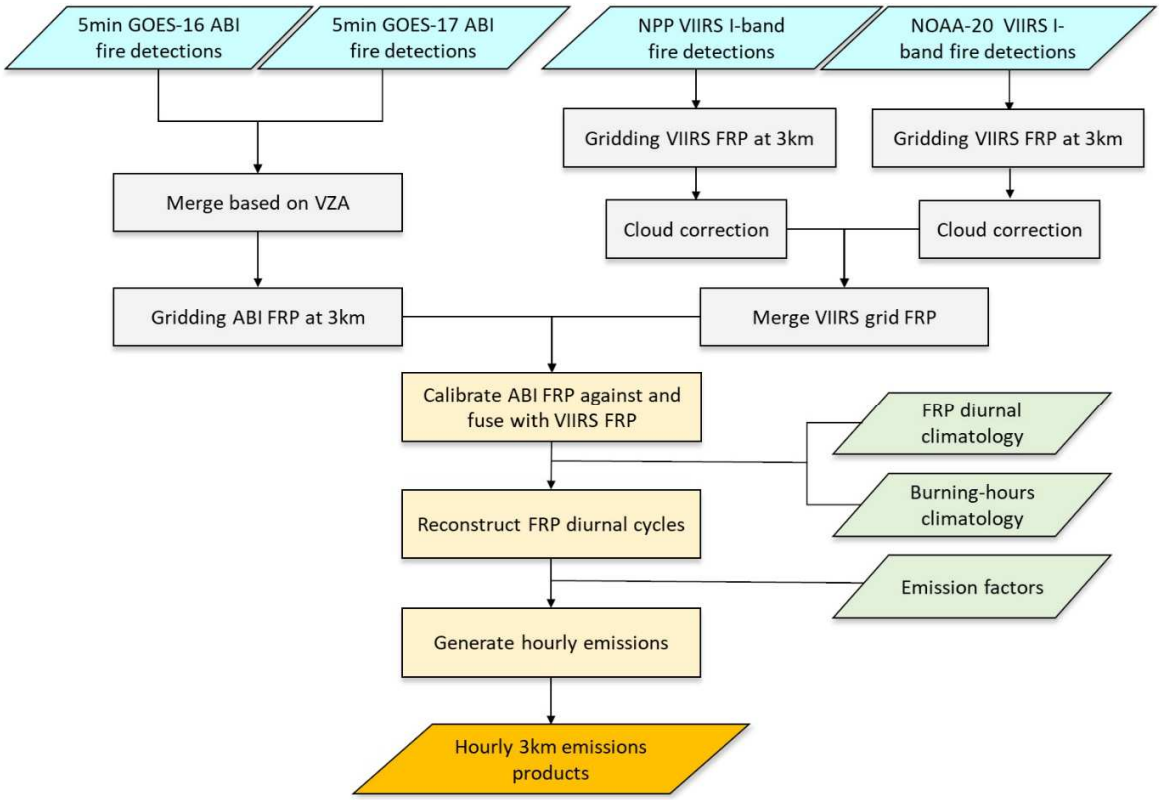

Figure 2. Flowchart of generating hourly 3 km emissions using ABI and VIIRS FRP. Note that the ABI and VIIRS fire detections are preprocessed data after removing false alarms based on a temporal filter and persistent anomaly flags (c.f. Sections 2.1 and 2.2).

3.1. Fusion of ABI FRP with VIIRS FRP

3.1.1. Gridding ABI and VIIRS FRP

ABI FRP from GOES-16 and GOES-17 and VIIRS FRP from Suomi NPP and NOAA-20 were first merged and gridded at 3km separately. Because GOES-16 and GOES-17 observe fires across the CONUS simultaneously in opposite directions, ABI fire detections from the two satellites were merged based on satellite VZA. Specifically, for a given fire event observed by the two satellites at the same time, fire detections with smaller VZAs were selected. The merged fire detections have a VZA less than 60° (with a pixel area ≤ 9 km^2) in most areas of the CONUS except a small fraction of the northeastern Montana State where both GOES-16 and GOES-17 have a VZA varying from 60° - 65°. The pixel-level FRP from legacy GOES satellites (e.g., GOES-13 and GOES-15) tended to be overestimated if a VZA was larger than 50° (Li et al., 2019) due to the contribution of non-fire background radiances (Schroeder et al., 2010). To examine if this issue also occurs in ABI FRP, we compared ABI FRP from GOES-16 and GOES-17 in four wildfires that occurred during the 2020 fire season in the western CONUS. For these fires, GOES-16 VZA varied from 53° to 64° (a pixel area of 7.6 - 9.6 km^2) and GOES-17 VZA changed very slightly between 46° and 50° (a pixel area of 6.3 – 6.9 km^2). We found that ABI FRP from the two satellites were comparable, with a small difference of 1% (Figure 3), which suggests that ABI FRP variation with VZA was negligible over the CONUS. Thus, the pixel-level FRP retrievals of the merged ABI fire detections that were observed at the same time and the same 3km grid were summed up, with each grid further classified by land cover and ecoregion maps. Note that the 3 km grids were mapped based on coordinates (i.e., longitude and latitude) with an interval of 0.03 degree. As a 3 km grid covered approximately 1 – 1.5 ABI pixels, we assumed that the grid was fully clear or totally cloudy if an ABI fire detection was

provided with valid FRP retrieval (FRP > 0 MW) or was flagged as cloud contaminated, respectively. The cloud-contaminated detections were considered as temporal gaps with missing FRP values in the FRP diurnal cycle.

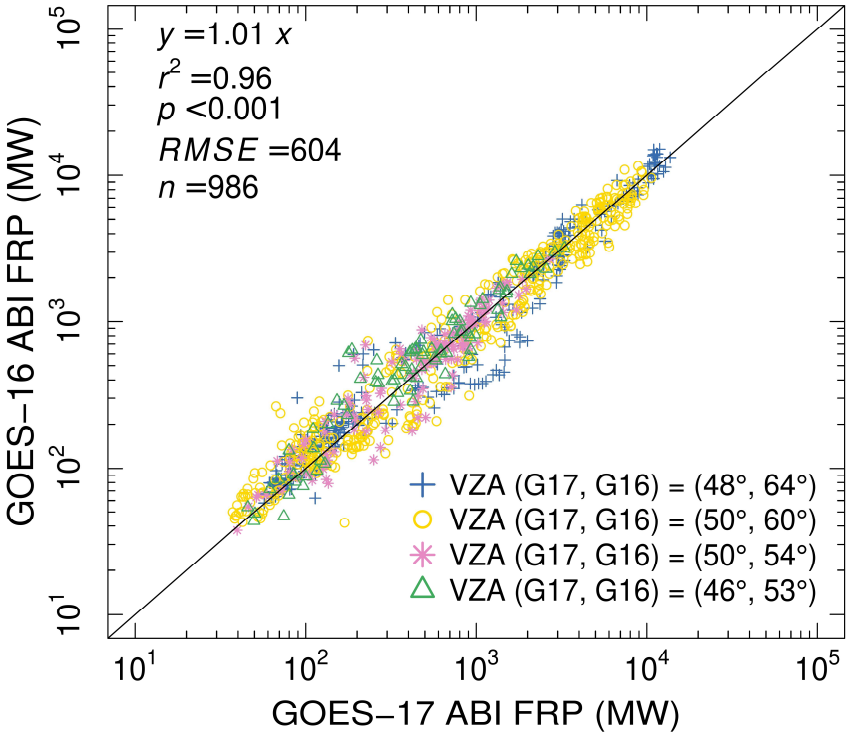

Figure 3. Comparison of GOES-16 and GOES-17 ABI FRP in four fires in 2020. Among these fires, GOES-17 VZA changed slightly between 46° and 50° while GOES-16 VZA varied largely from 53° to 64°, as shown in the VZA legend (for GOES-16). G17 and G16 in legend are abbreviations for GOES-17 and GOES-16, respectively. Each sample represents total FRP in a fire observed by both satellites at the same time.

The FRP at a 375 m pixel from Suomi NPP and NOAA-20 VIIRS fire detections was also aggregated to 3 km grids based on the location of a VIIRS pixel center at each VIIRS

overpass time separately, and further classified using the land cover and ecoregion maps. Because VIIRS could miss fire observations due to cloud obscuration, it is commonly assumed that fire burning condition under clouds is the same as that in clear-sky condition (Darmenov et al., 2015; Kaiser et al.; Giglio, 2007). However, this assumption of linear cloud correction could result in significant FRP overestimations if cloud fraction is very large. For the RAVE algorithm, the aggregated Suomi NPP and NOAA-20 VIIRS FRP for a given grid at an observation time was separately adjusted by assuming burning condition under clouds was nonlinearly correlated to the cloud fraction:

$$FRP^V = \frac{FRP^V_{agg}}{1-\beta+\alpha\times\beta^2} \quad (1)$$

where FRP^V_{agg} and FRP^V are the grid VIIRS FRP (unit: MW) before and after cloud correction; β is cloud fraction; and α is a coefficient that is set as 0.25 based on a set of tests. To further avoid FRP overestimation, cloud correction was not conducted in grids if the cloud fraction was larger than 95%. Then, the cloud-corrected grid VIIRS FRP from Suomi NPP and NOAA-20 were merged based on observation times.

3.1.2. Calibrating and Fusing ABI FRP with VIIRS FRP

The grid ABI FRP is calibrated against the grid VIIRS FRP because ABI FRP is potentially underestimated due to the omission of small and/or cool fires. This calibration is performed in a spatiotemporal-variant way using Eq. (2):

$$\overline{FRP^A_t} = FRP^A_t \times (1+r) \quad (2)$$

where, at observation time t, FRP_t^A is the cloud-corrected grid ABI FRP (unit: MW, as in Eq. (1)); $\overline{FRP_t^A}$ is the calibrated grid ABI FRP using a calibration factor r (unitless).

The calibration factor r is computed using Eq. (3) based on the contemporaneous grid ABI and VIIRS FRP values by assuming that the of ABI FRP underestimation is related to the magnitude of ABI FRP.

$$r = \frac{1}{n}\sum_{i=1}^{n}\left(\frac{FRP_i^V - FRP_i^A}{FRP_i^A}\right) \quad (3)$$

where, for a given grid in a specific day, n denotes the total number of FRP pairs observed by both ABI and VIIRS contemporaneously (within ±2.5 minutes) during the day; FRP_i^V and FRP_i^A are the ith pair of the contemporaneous grid VIIRS FRP (cloud corrected) and grid ABI FRP, respectively.

The calibration factor r varies among grids and days; this has been demonstrated to be robust in improving the 2-km Himawari-8 AHI FRP relative to VIIRS FRP (Li et al., 2021a). Note that calibration factor cannot be computed when VIIRS FRP observations are not available at all in a given day due to obscuration of clouds or forest canopies or due to instrument anomalies. Although such cases are very few, we still developed fixed calibration factors to adjust ABI FRP. The constant factors are calculated using empirical relationships derived by comparing contemporaneous VIIRS FRP from Suomi NPP and NOAA-20 and GOES-16 ABI FRP over 100 fires that burned in 2020 across an ABI VZA range of 30° - 60° (Figure 4).

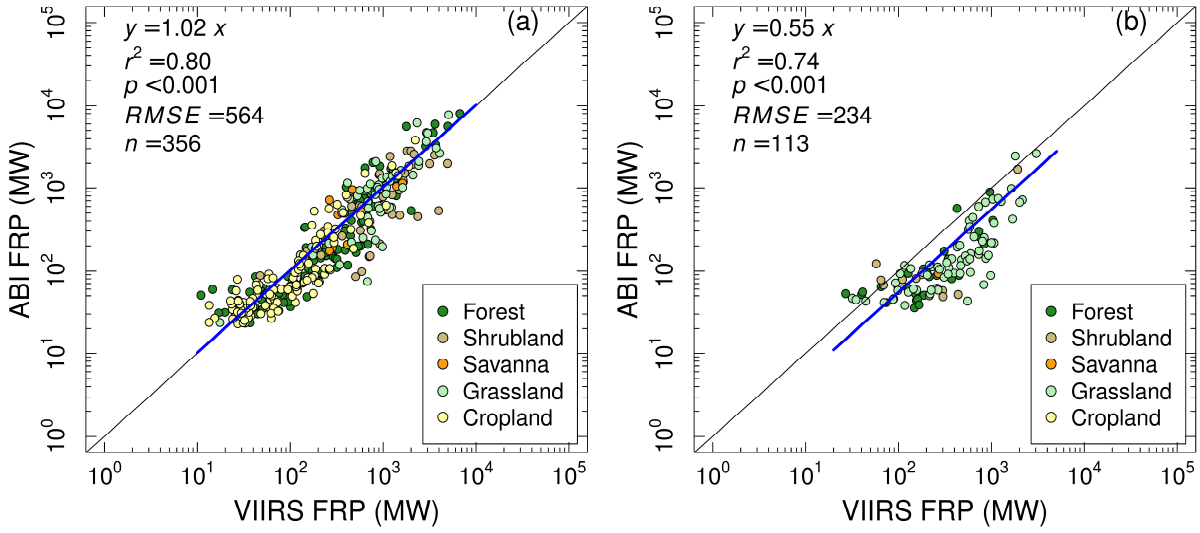

461

462 **Figure 4.** Comparison of contemporaneous ABI and VIIRS FRP in fire clusters. (a) Daytime and
463 (b) nighttime. Each sample represent FRP observed by GOES-16 ABI and Suomi-NPP or
464 NOAA-20 VIIRS contemporaneously (within ±2.5 min).

465

466 The calibrated grid ABI FRP and the grid VIIRS FRP were fused to generate ABI-VIIRS
467 FRP time series as following:

468 $$FRP_t^f = w_1 \times FRP_t^V + w_2 \times \overline{FRP_t^A} \quad (4)$$

469 where for a given grid at observation time t, FRP_t^f, FRP_t^V, $\overline{FRP_t^A}$ are the fused ABI-VIIRS
470 FRP, the cloud-corrected grid VIIRS FRP, and the calibrated ABI FRP (Eq.(2)), respectively;
471 and w_1 and w_2 are weights to combine VIIRS and ABI FRP. When VIIRS FRP is available (with
472 or without ABI FRP), $w_1 = 1$ and $w_2 = 0$; and when only ABI FRP is available, $w_1 = 0$ and $w_2 = 1$.

473

3.2. Reconstruction of FRP Diurnal Cycles

3.2.1. Building FRP Diurnal Climatologies

FRP diurnal climatologies were established to fit temporal gaps in the fused ABI-VIIRS FRP. As landscape-scale fire activities and characteristics (e.g., intensity, spread speed, and burning hours) are controlled by fuels, weather, and topography (Pyne et al., 1996), we built FRP diurnal climatologies for five main land cover types in 11 ecoregions using ABI FRP retrievals from GOES-16 from 2018-2020 and GOES-17 in 2020. An FRP diurnal climatology was established in three steps. First, for a given land cover type in a specific ecoregion, the gridded ABI FRP classified by land cover and ecoregion maps was binned every 5 minutes. Second, a mean FRP was calculated in each bin after removing a small number of outliers that were determined based on the density probability of FRP samples following Li et al. (2019). Third, the 5-minute mean FRP time series were fitted using the Discrete Fourier Transform (DFT) following Giglio (2007) and Zhang et al. (2012). Note that when the number of ABI FRP samples was insufficient for a given land cover type in a specific ecoregion, the associated FRP diurnal climatology was not derived.

Figure 5 illustrates the derived land cover-ecoregion-specific FRP diurnal climatologies in 3km grids. Overall, all diurnal climatologies display a similar pattern, with decreasing FRP from midnight to early morning, then increasing and peaking between 12 PM and 4 PM, and then decreasing again gradually. Nevertheless, FRP diurnal climatology in the same ecoregion varies among five land cover types. For example, in the deserts ecoregion, FRP climatologies in forest and savanna show stronger variations than other land cover types and the associated peak-time mean FRP are relatively larger (Figure 5a, c, f and h). Further, FRP diurnal climatology in the same land cover type changes in peak time and FRP magnitude among different ecoregions. In

497 forest, for example, climatological FRP peaks latest in the forested mountains ecoregion and
498 earliest in the temperate forest ecoregion (Figure 5a); and the peak-time climatological FRP is
499 the largest in the forested mountains ecoregion and the smallest in the temperate forest ecoregion
500 (Figure 5f). Such large differences in climatological FRP are also observed in the croplands
501 (Figure 5e, j). Among the five land cover types, the peak times of the FRP diurnal climatologies
502 in Savanna are very close (Figure 5h). The difference in mean FRP (Figure 5f-j) is likely related
503 to several factors, including but not limited to fire intensity, sensitivities of fire detection
504 algorithms, and observing areas in different land cover types and ecoregions.

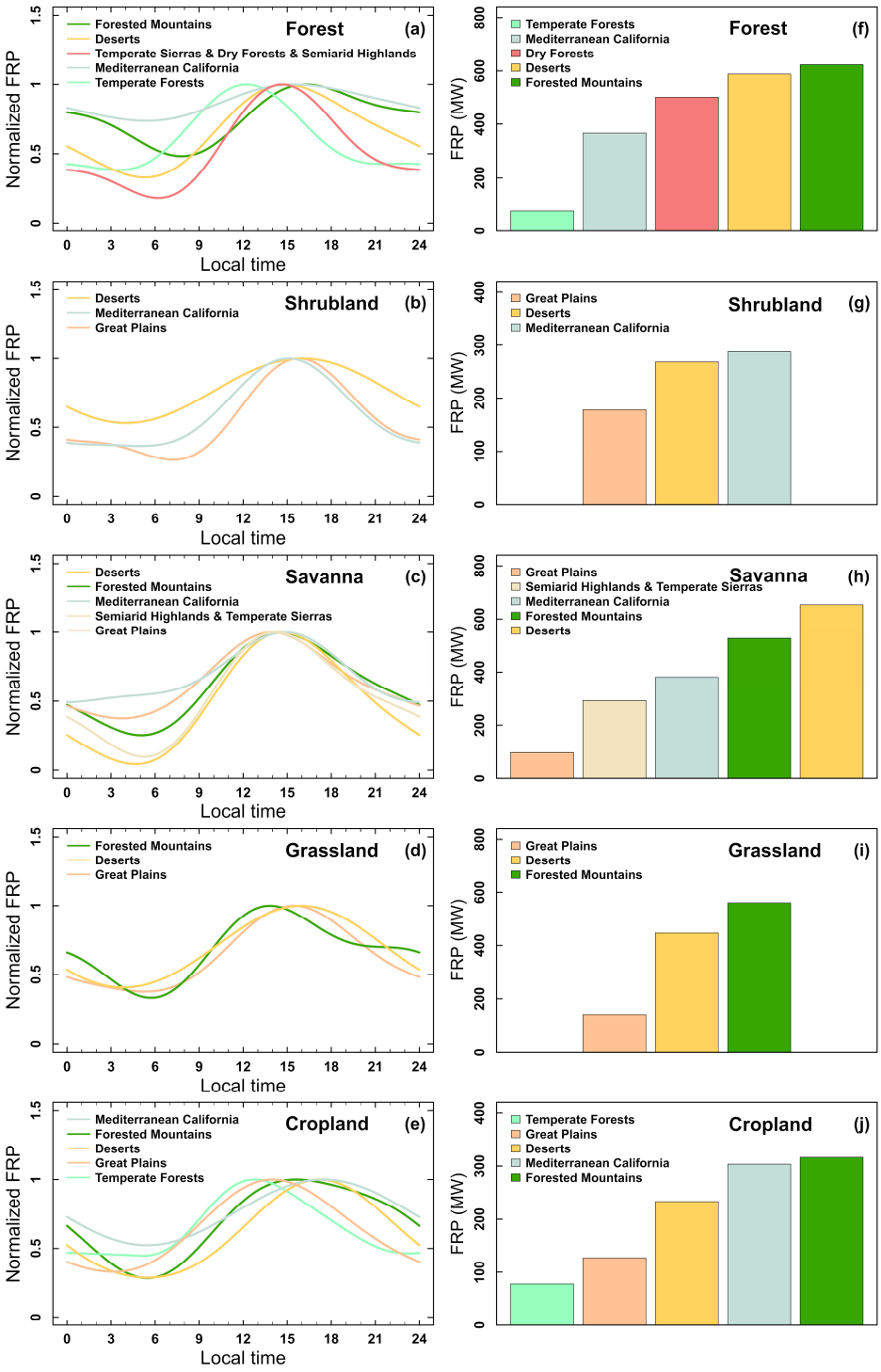

505

506 **Figure 5.** The land cover-ecoregion-specific FRP diurnal climatologies derived from GOES-16

507 and GOES-17 ABI FRP observations. The left column (a-e) shows the normalized diurnal FRP

in five land cover types: forest, shrubland, savanna, grassland, and cropland. Each normalized diurnal curve was obtained by calculating the ratio of the diurnal mean FRP values to the peak-time mean FRP value. The right column (f-j) shows the associated peak-time mean FRP in the five land cover types.

Climatological burning hours or diurnal burning durations were also calculated for the same land cover type in a specific ecoregion to determine the possible fire burning length. Specifically, for a given land cover type in a specific ecoregion, the 5th and 95th percentiles of the observation hours in the density probability of FRP samples described above were calculated as the climatological start and end burning hours, respectively.

3.2.2. Reconstructing FRP Diurnal Cycles

FRP diurnal cycles are reconstructed by filling temporal gaps in the fused ABI-VIIRS FRP time series. A temporal gap occurs at specific observation times when the sensors miss fire observations or when the fire products fail to retrieve valid FRP for specific fire observations. Although the ABI instrument observes fires across the CONUS every 5 minutes, it could miss fire observations in some observing times due to the obscuration of occasional clouds, very thick smoke plumes, and forest canopies. Of course, the instrument could have no fire observations at all in a specific grid if clouds fully cover the grid and are persistent all day, which can hardly be dealt with due to the lack of information on under-cloud burning conditions and thus is not considered in the following analyses. Furthermore, FRP could be missing or invalid if the fire products fail to characterize non-fire background or the sensors are saturated in extremely intense fires. For example, while FRP is sometimes provided by the ABI fire product for saturated pixels, the estimated FRP is known to be low and thereby has been considered an

invalid FRP (or a temporal gap). The missing FRP in temporal gaps are predicted using the reconstructed FRP diurnal cycle. For a grid in which ABI and/or VIIRS observed fires during a specific day, an FRP diurnal cycle is reconstructed in two steps. First, temporal gaps, which refer to time slots when the valid ABI-VIIRS FRP is not available, are located. A gap could appear prior to or/and after a valid fused FRP; and its length could vary from 5 minutes to several hours. Second, the missing FRP values in temporal gaps are predicted in two different ways. (1) For gaps shorter than one hour, missing FRP values are interpolated using the immediate neighboring valid FRPs. (2) Missing FRP values in gaps longer than one hour are predicted using FRP diurnal climatology and an optimal offset, which is based on the assumption that FRP diurnal cycles share similar shapes for a given land cover type in the same ecoregion (Li et al., 2019; Zhang et al., 2012). The optimal offset is calculated from a set of the valid ABI-VIIRS FRP and the corresponding climatological FRP values at the same time slots based on a least square method. It is then applied to shift FRP diurnal climatology to predict FRP missed in the temporal gaps. If without FRP values observed during a day but active fires are detected, the climatological FRP values are adopted. If FRP diurnal climatology is not available in the corresponding ecoregion, the climatology of the same land cover type from a neighboring ecoregion is used.

It is important to note that only parts of a given long gap are filled because fires might not burn continuously during the entire gap. For instance, fast-running grass or forest fires in the western CONUS could spread tens of kilometers in a day (Andela et al., 2019). In other words, those fires likely reside in a 3km grid only for several hours. Moreover, agricultural burnings and prescribed fires usually burn during some hours when fire weather is favorable and fires are manageable. Such fires could be very small and/or cool and detected by VIIRS only. Thus, we

554 use the climatological burning hours (c.f. Section 3.2.1) to determine the possible burn duration
555 of a long gap. We assume that fires burned one hour prior to and after a valid ABI-VIIRS FRP
556 observation if a long gap occurs during climatological burning hours; otherwise, a burning
557 duration of 30 minutes before and after a valid fused FRP observation is used. As a result, an
558 FRP diurnal cycle in a 3 km grid consisted of the gap-filled fused FRP.

559

560 3.3. Estimation of Biomass-burning Emissions

561 The consumed dry matter and emitted fire emissions are computed from the reconstructed
562 FRP diurnal cycles in 3km grids. For a given grid, hourly FRE is first calculated by integrating
563 FRP diurnal cycle during each hour, as expressed in Eq. (5).

564 $$FRE = \int_{t1}^{t2} FRP_t^d \, dt \tag{5}$$

565 where FRE is hourly total FRE (unit: MJ); FRP_t^d is the 5-minute FRP value from the
566 reconstructed FRP diurnal cycle (c.f. Section 3.2) at observation time t; and $t1$ and $t2$ denote the
567 first and last 5-minute observation time slots in the given hour, respectively.

568 Then, hourly total dry matter consumption and emissions of eight chemical species
569 (Table 2) are calculated for the RAVE product using equations 6 and 7 separately.

570 $$DM = FRE \times F_c \tag{6}$$

571 $$M_x = DM \times EF_x \tag{7}$$

where DM is hourly consumed dry matter (unit: kg); FRE is as in Eq. (5); F_c is the biomass combustion coefficient (unit: kg MJ^{-1}); M_x is hourly total mass (unit: kg) of emission species x; and EF_x is the emission factor (unit: kg kg^{-1}) of the species x.

FRE biomass combustion factors (F_c) in the CONUS wildfires was set as 0.368 kg MJ^{-1} that was obtained from field-based experiments (Wooster, 2005). The robustness of this value was verified in several laboratory and landscape measurements where the difference was less than 20% (Kremens et al., 2012; Li et al., 2018b; McCarley et al., 2020). Because RAVE algorithm is specific to the CONUS, emission factors (EF_x) were averaged from reported emission factor values for North American fires compiled in two recent emission factor datasets (Akagi et al, 2011; Andreae, 2019). Note that the global average value from Andreae (2019) was used directly if the number of studies for North America fires was less than three for a given species. The standard deviation (SD) was added to represent the EF uncertainty (Table 2).

Table 2. Emission factors (unit: g kg^{-1}) of eight chemical species

Emission species	Forest	Savanna, Shrubland, Grassland	Cropland
	mean (SD)	mean (SD)	mean (SD)
Carbon dioxide (CO2)	1598.5 (114)	1686.0 (112)	1585.0 (100)
Carbon monoxide (CO)	88.6 (22.2)	63.0 (14.7)	102.0 (33.0)
Particulate matter ($PM_{2.5}$)	12.8 (8.98)	7.17 (2.12)	6.26 (4.02)
Organic carbon (OC)	6.37 (3.30)	3.12 (0.92)	3.54 (3.34)
Nitrogen oxides (NO_x)	1.91 (1.82)	3.90 (1.50)	3.11 (1.57)
Ammonia (NH_3)	0.84 (0.72)	0.56 (0.53)	2.17 (1.27)
Sulfur dioxide (SO_2)	0.70 (0.48)	0.47 (0.44)	0.80 (0.42)

Black carbon (BC)	0.55 (0.40)	0.37 (0.20)	0.42 (0.28)

585

586

587 3.4. Emissions Evaluation

588 We evaluated the RAVE emission estimates produced in the CONUS using the Sentinel-
589 5P TROPOMI CO observations over individual fire events. CO is inert on the timescale of
590 smoke plume aging with an average lifetime of two months in the atmosphere, so it is a good
591 tracer of smoke plume transport (Streets et al., 2013; Yokelson et al., 2009).

592

593 3.4.1. Selecting Fire Samples

594 Fire events with isolated and fresh smoke plumes were chosen manually using
595 observations from multiple satellites. Because dilution of emissions in smoke plume is affected
596 mainly by smoke plume thickness and wind speed and direction (Hodshire et al., 2019; Hodshire
597 et al., 2021), this study focused on fresh smoke plumes to minimize the effect of dilution.
598 Specifically, we defined that a fresh smoke plume is emitted within 4 hours, as illustrated in
599 Figure 6. First, potential fire events were chosen by screening Suomi NPP VIIRS fire detections
600 and true-color imageries and Sentinel-5P TROPOMI CO data on NOAA JSTAR Mapper
601 (https://www.star.nesdis.noaa.gov/jpss/mapper/, last accessed on 12/01/2021). The JSTAR
602 Mapper, a public online tool, provides daily global maps of many products from different
603 satellites, including Suomi NPP and NOAA-20 VIIRS and Sentinel-5P TROPOMI. As the
604 observation time difference between Suomi NPP VIIRS and Sentinel-5P TROPOMI is 5 minutes,
605 VIIRS fire detections and true-color imageries were first used to locate fires in which the

606 associated smoke plumes were visually interpretable and not contaminated by clouds and other
607 smoke plumes. TROPOMI CO maps were then applied to refine these fire samples by removing
608 the ones in which (1) TROMOPI missed some CO observations due to strong water vapor close
609 to fire fronts or (2) smoke CO enhancement above background was very small (i.e., < 10 ppbv).
610 Second, the selected samples were further refined by examining the freshness of their
611 smoke plumes. For a given sample, a times series of ABI true-color imageries were first
612 composed from 5-minute ABI radiances (c.f. Section 2.2), which were observed within four
613 hours before TROPOMI's overpass. Then, the time series was examined to determine the start
614 time of the smoke plume. If the start time was found, the sample was considered as a qualified
615 one with a fresh plume. In this step, we noticed that some smoke plumes shown in the ABI true-
616 color image time series dispersed as wind direction changed, which might result in strong
617 dilution. Thus, these samples were also removed. As a result, a total of 27 fires in different land
618 cover types were selected during the period from April 2020 to March 2021, with an average
619 smoke age of two hours.

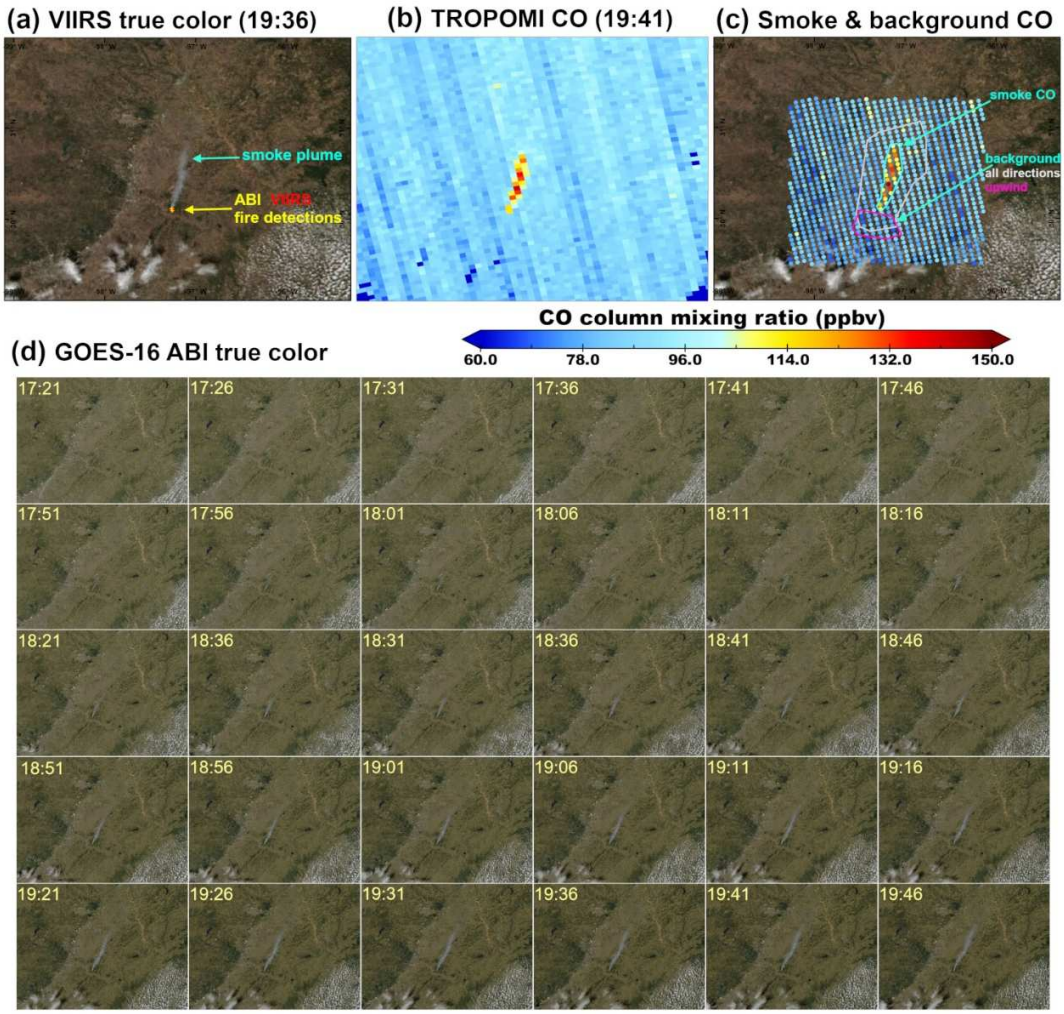

620

621 **Figure 6.** An example of fire sample selection. (a-d) show the process of choosing one fire event
622 based on TROPOMI CO observations and Suomi NPP VIIRS and GOES-16 ABI true-color
623 images and active fire detections. The fire occurred near Austin in South Texas (the United
624 States) on 10 December 2020. (a) Suomi NPP VIIRS true-color image with VIIRS and ABI fire
625 detections observed at 19:36 UTC and 19:41 UTC, respectively. (b) TROPOMI CO column dry
626 air mixing ratio (unit: parts per billion by volume or ppbv in short) observed at around 19:41
627 UTC, with smoke plume in warm colors. (c) Delineated smoke CO and background CO overlain
628 on the Suomi NPP VIIRS true-color image. The upwind and all-directions backgrounds are

629 delineated using white and pink polygons. (d) Time series of GOES-16 ABI true-color images
630 shows the evolution of the smoke plume during 17:21 – 19:46 UTC.

631

632 For each selected sample, TROPOMI CO observations of the smoke plume and
633 background were extracted separately. First, smoke CO observations were delineated manually
634 by referencing to the plume edges shown in VIIRS true-color imagery and CO enhancement
635 above background (Figure 6c). Then, the delineated smoke boundaries were buffered outward by
636 at least three TROPOMI CO pixels (i.e., ~21 km and ~16.5 km along the track and scan
637 directions) to extract background CO observations. In addition, CO observations in the upwind
638 region were also extracted to calculate background CO.

639

640 3.4.2. Comparing RAVE CO with TROPOMI CO

641 The total CO mass was calculated for each of the 27 selected fires using our FRP-based
642 hourly RAVE CO emissions and TROMOPI CO observations. For a given fire sample, the FRP-
643 based CO mass was aggregated from our hourly 3 km RAVE CO estimates (c.f. Section 3.3)
644 during the period from the start time of smoke plume to the Sentinel-5P overpass time. To
645 calculate the TROPOMI-based CO emissions, smoke and background CO observation were
646 extracted separately using the delineated plume and background boundaries. Because the
647 selected smoke plume samples were emitted only a few hours earlier than the TROPOMI
648 overpass, we assumed that CO oxidation and dilution are negligible. Then, the total CO mass
649 was calculated using CO enhancement above background as following:

650 $$M'_{co} = \sum_{i=1}^{n} (\rho_{sm}^{i} - \rho_{bg}) \times A^{i} \times M \quad (8)$$

where M'_{co} is the total mass of CO emissions for a given fire sample; ρ^i_{sm} and A^i are the observed CO total column (unit: mol m^{-2}) and pixel area (unit: m^2) of the *i*th smoke pixel; ρ_{bg} denotes the average column density of clear background pixels; and M is the molecular mass of CO (M = 28.01 g mol^{-1}).

Non-smoke background emissions are commonly calculated from upwind observations (Ichoku and Ellison, 2014; Jin et al., 2021; Lu et al., 2019). To examine the effect of background pixels on emissions estimates, we calculated background CO using background observations of (1) upwind and (2) all directions, respectively. The total CO mass was calculated using two different background CO separately using Eq. (8) and compared their differences (c.f. Section 5.2). Finally, the FRP-based and the TROPOMI-based total CO mass estimates (with the upwind background CO) are compared statistically over the 27 selected fire events.

3.5. Comparing RAVE with Other Emissions Inventories

Because fire-emitted $PM_{2.5}$ emissions are commonly used to investigate the effect of biomass burning on air quality (Jaffe et al., 2020; Li et al., 2021b), we also compared the RAVE $PM_{2.5}$ emissions with other eight emissions inventories (Table 1). First, we explored discrepancies in the annual total $PM_{2.5}$ and seasonal variations across the CONUS. Then, we also examined the total $PM_{2.5}$ emissions from different inventories in California's top five largest wildfires in the 2020 fire season. Information of the five largest wildfires were obtained from the NIFC. The perimeters of these fires were delineated using the 30m Landsat-8 burned area data (c.f. Section 2.5).

4. Results

4.1. Spatial Patterns of Biomass Consumption and Fire Emissions

Fires across the CONUS burned a total of approximately 221 Tg dry matter, and emitted 2.25 Tg $PM_{2.5}$, 360 Tg CO_2, 18 Tg CO, 1.58 Tg OC, 0.6 Tg NO_x, 0.2 Tg NH_3, 0.14 Tg SO_2, and 0.11 Tg BC from April 2020 - March 2021 (Table 3). The biomass consumption and fire emissions showed spatial variability, which was large and sparsely clustered in the western U.S. but small and widespread in the Great Plains and the southeast U.S. (Figure 7). The consumed dry matter was 181 Tg (82%), 22 Tg (10%), and 18 Tg (8%), respectively, in the three regions; the corresponding $PM_{2.5}$ emissions were 1.94 Tg (86%), 0.15 Tg (7%), 0.16 Tg (7%) $PM_{2.5}$. In the western U.S., fires in the three coastal states (California, Oregon, and Washington) consumed 115 Tg dry matter and released 1.3 Tg $PM_{2.5}$ emissions, accounting for approximately half of the totals across the entire CONUS. In the Great Plains, fire emissions in Kansas, Oklahoma, and North Dakota accounted for ~50% emissions of the region. In the eastern U.S., emissions were limited in the northeast but dominated in the southeast. Across the region, the emissions accounted for 13% in the Mississippi Alluvial Plain and ~50% in the three neighboring states of Florida, Georgia, and Alabama.

Biomass consumption and fire emissions also differ among land cover types (Table 3). Forest fires contributed 56% to the total biomass consumption and more than half to the total emissions for most species, with 41% (minimum) to the total NO_x and 84% (maximum) to the total OC. Among the other four land cover types, fire emissions of CO_2, CO, $PM_{2.5}$, OC, and NO_x were the smallest in shrubland and similarly large in savanna, grassland, and cropland. Interestingly, agriculture burnings were the second largest source for the emissions of NH_3, SO_2, and BC.

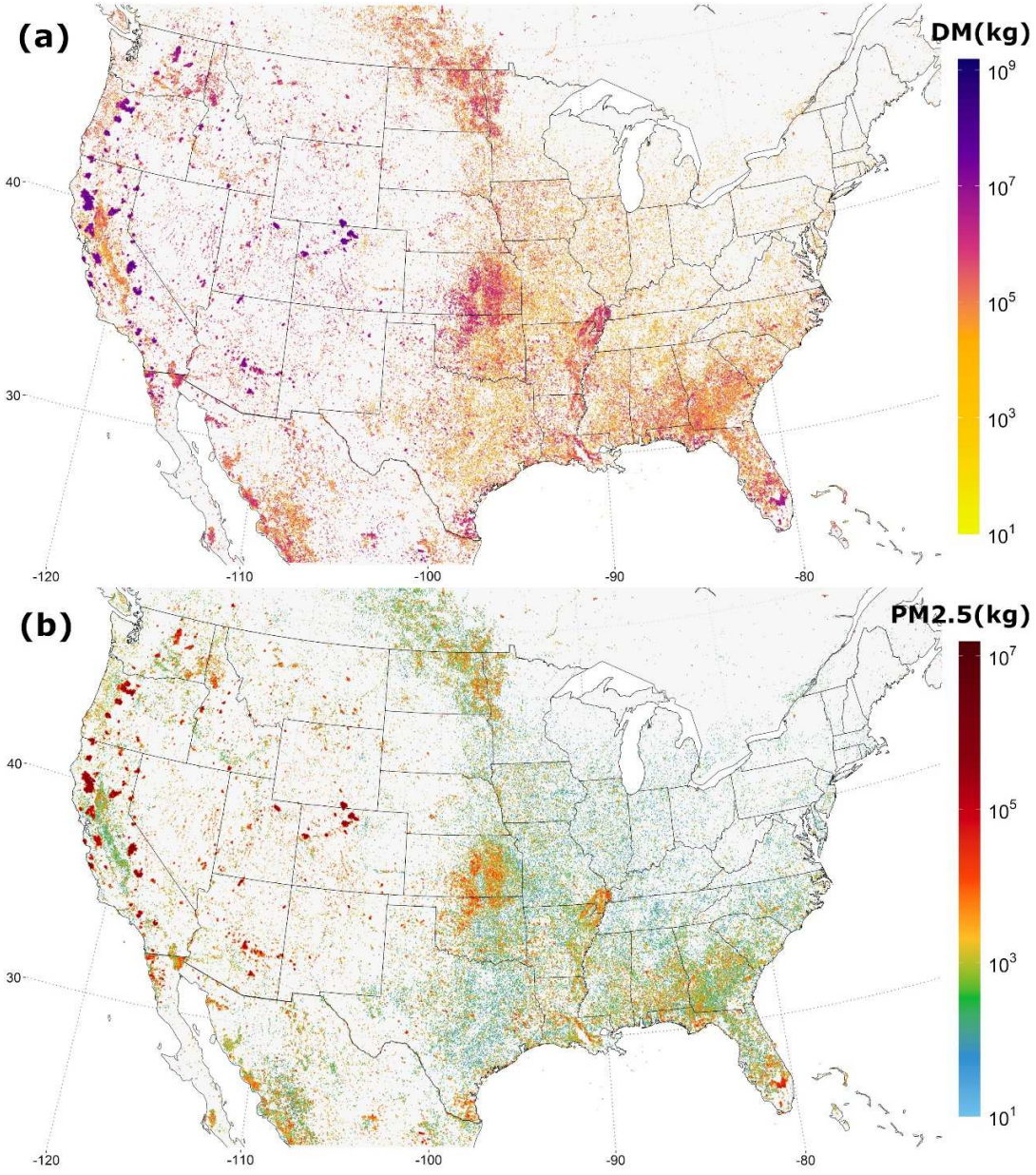

697

698 **Figure 7.** Annual total dry matter (a) and $PM_{2.5}$ emissions (b) in 3 km grids from April 2020 –

699 March 2021.

700

701

Table 3. Annual total mass (unit: Gg) of consumed dry matter and eight emission species in five main land cover types.

Emission species	Forest	Shrubland	Savanna	Grassland	Cropland	Total
DM	124,712	18,739	29,609	23,195	25,091	221,346
CO2	199,609	31,569	49,922	38,988	39,769	359,857
CO	10,974	1,190	1,865	1,498	2,559	18,086
$PM_{2.5}$	1,580	134	212	172	157	2,255
OC	1,335	49	77	70	57	1,588
NO_x	244	72	115	88	78	597
NH_3	103	10	16	13	54	196
SO_2	86	9	13	11	20	139
BC	68	7	11	9	19	114

4.2. Temporal Variations in Fire Emissions

The temporal variations are explained using $PM_{2.5}$ emissions as an example because they are very similar among various emissions species. Figure 8 illustrates the hourly variations of $PM_{2.5}$ emissions in five land cover types across the CONUS. The diurnal pattern is similar in all the five land cover types: limited between midnight and early morning, increasing sharply after 9 AM, peaking around 2 PM – 3 PM, and then decreasing gradually until midnight (Figure 8a). Daytime (6 AM – 6 PM local time) fires account for 91%, 83%, 79%, and 73% of daily total $PM_{2.5}$ in cropland, shrubland, grassland, and savanna, respectively (Figure 8a). In forest, daytime

714 fires explain 95% of daily $PM_{2.5}$ in the eastern U.S., whereas daytime and nighttime fires are
715 respectively responsible for 64% and 36% of daily $PM_{2.5}$ in the western U.S. (Figure 8b).

716 The hourly emissions variations around peak time differ among five land cover types
717 (Figure 8). In the daytime, emissions in all land cover types except Forest peak at 2 PM while
718 forests in the eastern and western U.S. peak at 1 PM and 3 PM, respectively. Cropland and
719 Forest in the east CONUS have the largest hourly variation during 1-2 hours before and after the
720 associated peak hour, showing relatively narrow and sharp peaks. On the contrary, Savanna and
721 Forest in the western U.S. have the smallest hourly variation, presenting relatively wide and flat
722 peaks. At night, all land cover types show a flat peak at 3 - 4 AM, which is the most pronounced
723 in Forest relative to the daytime peak.

724

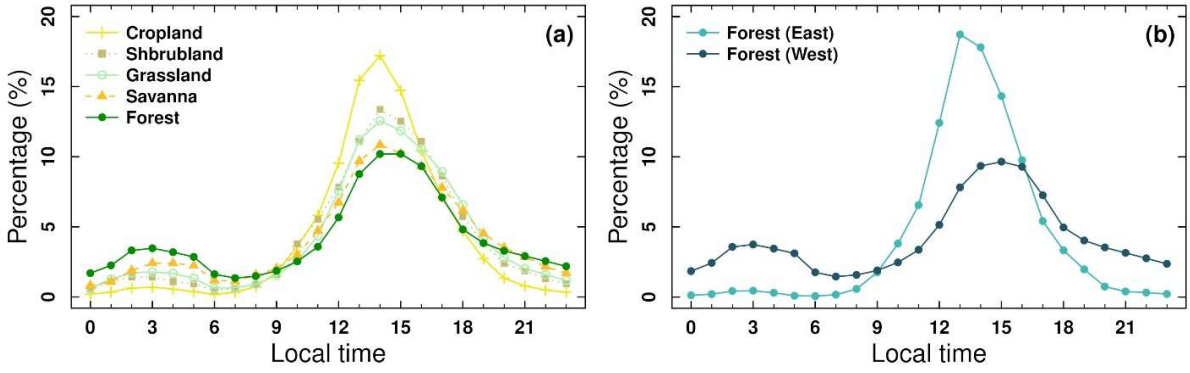

725

726 **Figure 8.** Land cover-specific diurnal patterns of $PM_{2.5}$ emissions. $PM_{2.5}$ diurnal patterns in (a)
727 five land cover types across the whole CONUS, and (b) Forest across the west and east CONUS.

728

729 Hourly emissions vary largely in large wildfires. Figure 9 shows the time series of hourly
730 $PM_{2.5}$ emissions in three largest wildfires (August Complex Fire, Creek Fire, and North Complex
731 Fire) in California in 2020. In the largest August Complex Fire, for example, the diurnal pattern
732 is generally similar during September 4-6, while it varies strongly in the following three days

733 when $PM_{2.5}$ is very high (Figure 9a). Strong hourly variations are also shown in the Creek Fire
734 during September 5-7 (Figure 9b). Moreover, in these fires, nighttime fire emissions are strong
735 and daily emissions peak time varies very largely between 11 AM and 4 PM (Figure 9).

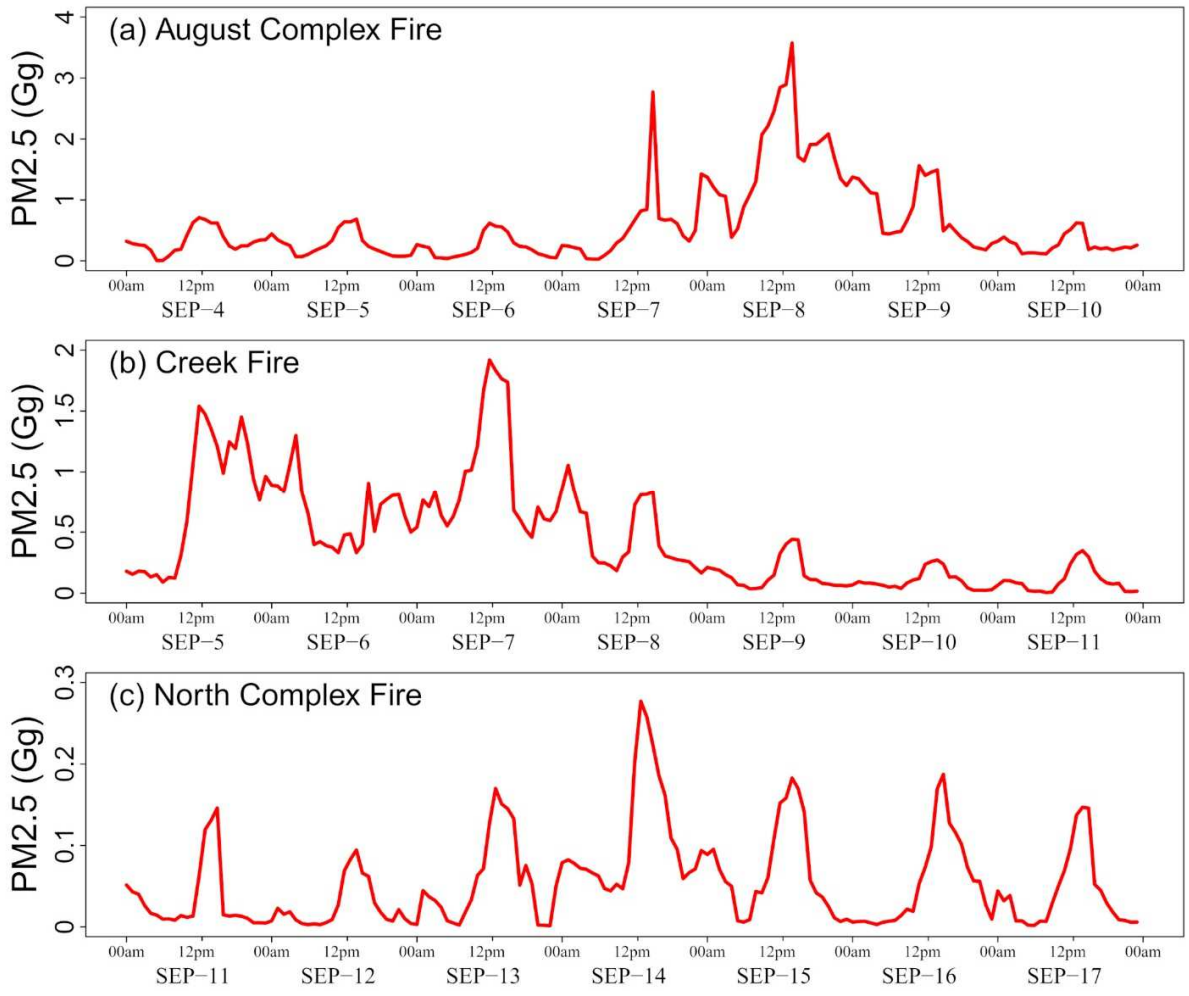

736

737 **Figure 9**. Hourly total $PM_{2.5}$ emission from three California largest wildfires in 2020. (a) The
738 August Complex Fire during the week from 4 – 10 September 2020, (b) the Creek Fire during
739 the week from 5-11 September 2020, and (c) the North Complex Fire during the week from 11-
740 17 September.

741

Figure 10 shows the monthly variations of $PM_{2.5}$ emissions in five land cover types. Strong seasonal variation is seen in forest, savanna, grassland, and shrubland, where emissions are high in summer and early autumn and low in winter and spring. For instance, forest and savanna $PM_{2.5}$ during three months from August-October 2020 amount to 87% and 74% of the annual totals, respectively. Especially, in forest, September 2020 alone explains 60% of the annual total $PM_{2.5}$. In contrast, cropland shows a very small seasonal variation although winter emissions are also slightly lower than the other seasons. Moreover, cropland is the largest source of $PM_{2.5}$ emissions during the winter and spring months relative to the other four land cover types.

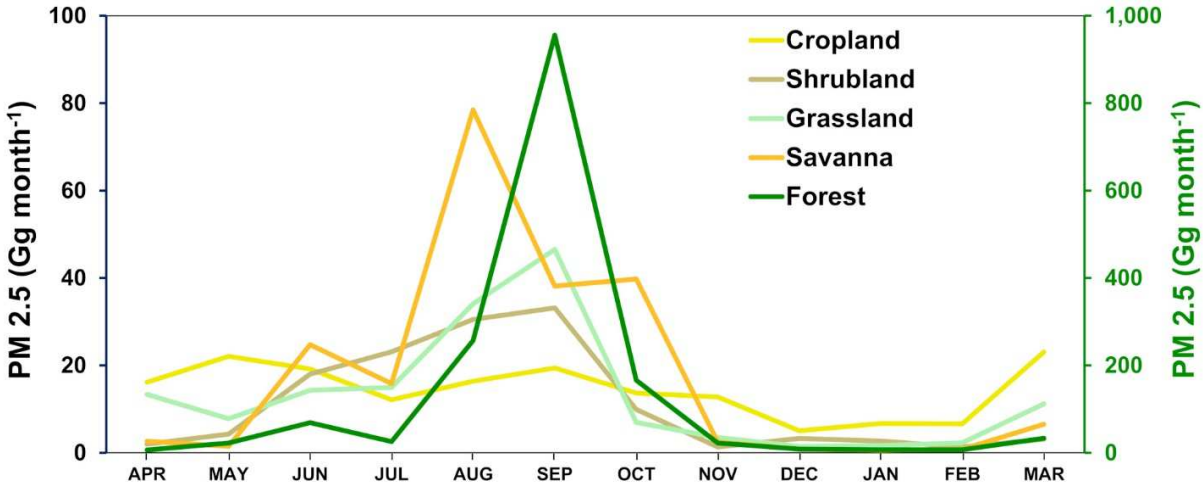

Figure 10. Monthly total mass of $PM_{2.5}$ emissions in five land cover types during one year from April 2020 to March 2021. Note that forest $PM_{2.5}$ uses the second y-axis on the right.

4.3. RAVE CO versus TROPOMI CO in the Selected Fires

Figure 11 shows the comparison of RAVE CO emissions with TROPOMI CO emissions for the 27 selected fires. These fires occurred in five different land cover types across the CONUS (Figure 11a). Over the 27 selected fires, the mean CO enhancement varied from 17 to

302 ppbv, with an average of 81 ppbv (Figure 11b). The largest enhancement is seen in a forest fire that occurred in Southern California, where the CO in the smoke on average was 300% higher than the upwind background CO. The CO enhancement in the western U.S. is much higher than the eastern U.S. (133 ppbv vs. 51 ppbv), whereas the background CO in the western U.S. is slightly lower than the eastern U.S. (76 ppbv vs. 104 ppbv). This pattern is consistent with those of CO observations from other satellites (Jiang et al., 2018b).

The RAVE CO agrees well with TROPOMI CO overall in the selected fires (Figure 11c). Over the 27 fires, the total mass of the FRP-based RAVE CO varied from 0.12 to 9.56 Gg, which is similar to the range (0.15 – 9.48 Gg) of TROPOMI CO. The RAVE CO and TROPOMI CO are significantly correlated (R^2=0.94, $p < 0.001$), with a root mean square error (RMSE) of 0.56. Overall, the RAVE CO, on average, is 11% (22% at a 95% confidence interval) higher than TROPOMI CO.

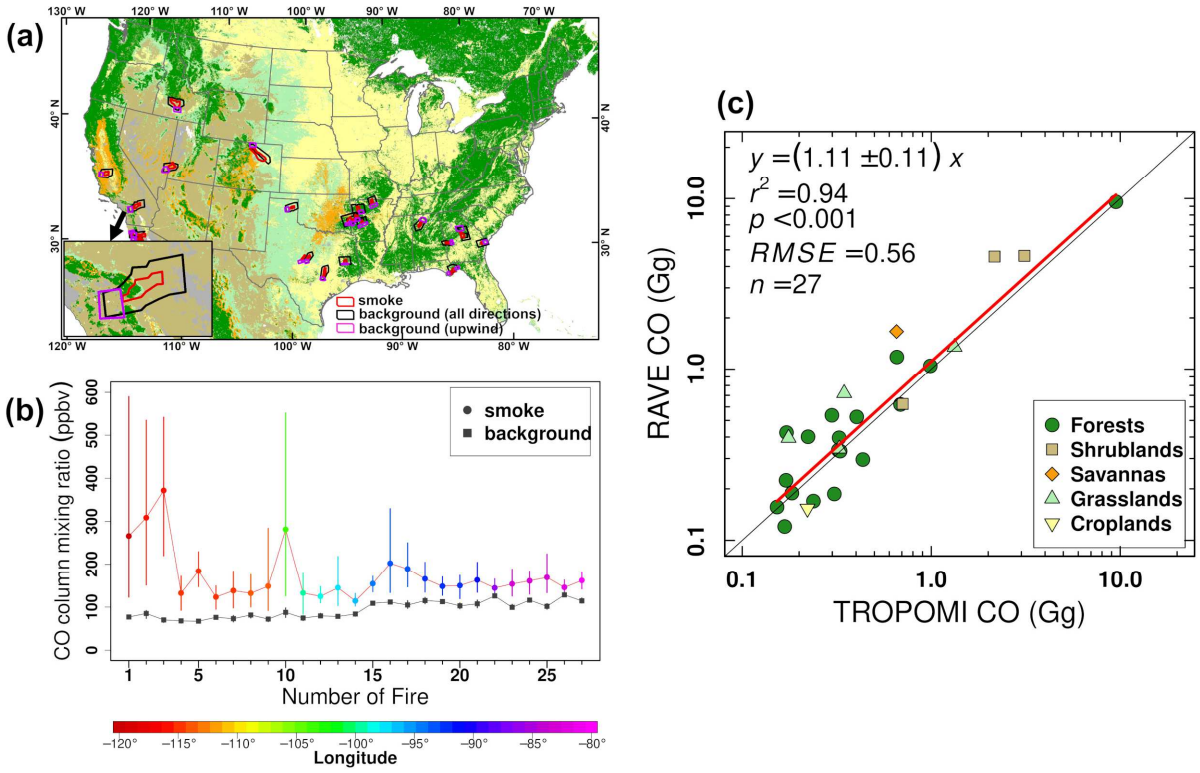

772

773 **Figure 11**. Comparison of CO emissions in the selected fires. (a) Distribution of the selected 27
774 fires overlain on the land cover map (as in Figure 1a). The inset shows a fire example. Red, black,
775 and purple polygons delineate TROPOMI CO observations in smoke plume and background. (b)
776 The TROPOMI CO column mixing ratio of smoke plume and upwind background in the selected
777 fires (colored by longitude), with their mean values denoted by circles and squares, respectively.
778 Error bars show the 20th and 80th percentile CO column mixing ratios. (c) Comparison of
779 RAVE and TROPOMI CO mass in the selected fires.

780

781 4.4. Comparison of RAVE with Other Emissions Products

782 The annual total mass of the RAVE $PM_{2.5}$ emissions agrees with some inventories but
783 differs largely from a few others (Figure 12a). Among eight inventories, the annual $PM_{2.5}$ varied

784 from 1.55 to 9.48 Tg. The annual RAVE $PM_{2.5}$ is slightly larger (<8%) than WFEIS2.0 and
785 GFED4s, and about 45% larger than GFAS1.2. However, the RAVE emissions are smaller than
786 the other four inventories, with a factor of 1.2, 1.5, 4.1, and 4.2, respectively, relative to
787 FEER1.0, FINN2.4, QFED2.5, and GBBEPx4. Note that the FINN2.4 $PM_{2.5}$ is only from April
788 to December.

789 The monthly total mass of $PM_{2.5}$ further shows very large discrepancies among eight
790 inventories (Figure 12b). All inventories display a generally similar seasonal pattern. Among all
791 inventories, monthly $PM_{2.5}$ from QFED2.5 and GBBEPx4 are the highest while GFED4s is the
792 lowest in most months. The discrepancy between inventories is relatively small in the period
793 from August – October than the other months, where the minimal and maximal monthly $PM_{2.5}$
794 difference varies from a factor of 7 in September to 39 in December 2020, with an average of 16.
795 Compared with the other seven inventories, the RAVE monthly $PM_{2.5}$ differs by a factor of up to
796 9 in November, but 1.5 to 4.4 in the peak month (September 2020).

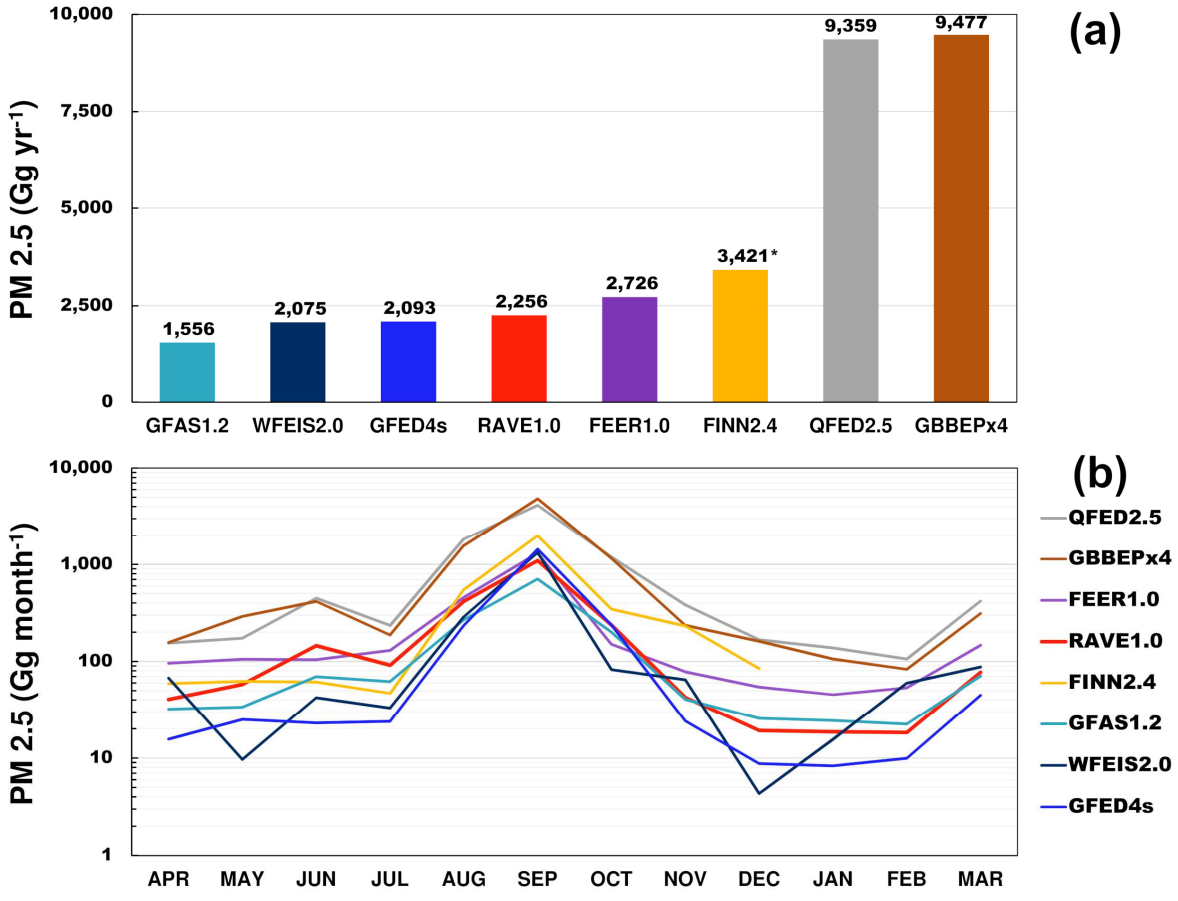

797

798 **Figure 12.** $PM_{2.5}$ emissions in eight inventories. (a) Annual total $PM_{2.5}$ and (b) monthly total
799 $PM_{2.5}$. Y-axis in (b) uses a logarithmic scale. Note that FINN2.4 $PM_{2.5}$ emissions only account
800 for 9 months from April – December 2020 because it was not available for 2021 when the
801 analysis was performed.

802 Large discrepancies in $PM_{2.5}$ emissions are also observed in individual large wildfires
803 (Table 4 & Figure 13). Among the five largest wildfires during the study period, nearly all
804 inventories report the highest $PM_{2.5}$ in the August Complex Fire and the lowest in the SCU
805 (Santa Clara Unit) Complex Fire. Yet, the discrepancy among all inventories is as large as a
806 factor of 5 – 18 in the five fires. Moreover, except for QFED2.5 and GBBEPx4 with the highest
807 estimates, the other six inventories do not show a consistent larger or smaller estimate. Among

all inventories, the RAVE $PM_{2.5}$ is comparable with CARB, with a difference < 30% in four fires, but smaller than QFED2.5 and GBBEPx4 by a factor of up to 6 (Table 4). Furthermore, the spatial patterns of $PM_{2.5}$ emissions in the largest August Complex Fire also differ widely among inventories (Figure 13).

Table 4. The total mass of $PM_{2.5}$ (unit: Gg) from California's five largest wildfires in 2020.

Fire Name	Fire Area (km^2)*	CARB	GFAS1.2	GFED4s	RAVE1.0	FEER1.0	FINN2.4	QFED2.5	GBBEPx4
August Complex	4,179	283	164	455	274	478	703	1171	1211
SCU Complex	1,605	26	25	11	35	6	10	103	71
Creek Fire	1,537	146	107	186	153	206	51	623	915
LNU Complex	1,470	21	29	48	48	85	33	157	241
North Complex	1,290	102	53	232	76	128	216	274	284

* Fire area information was obtained from NIFC.

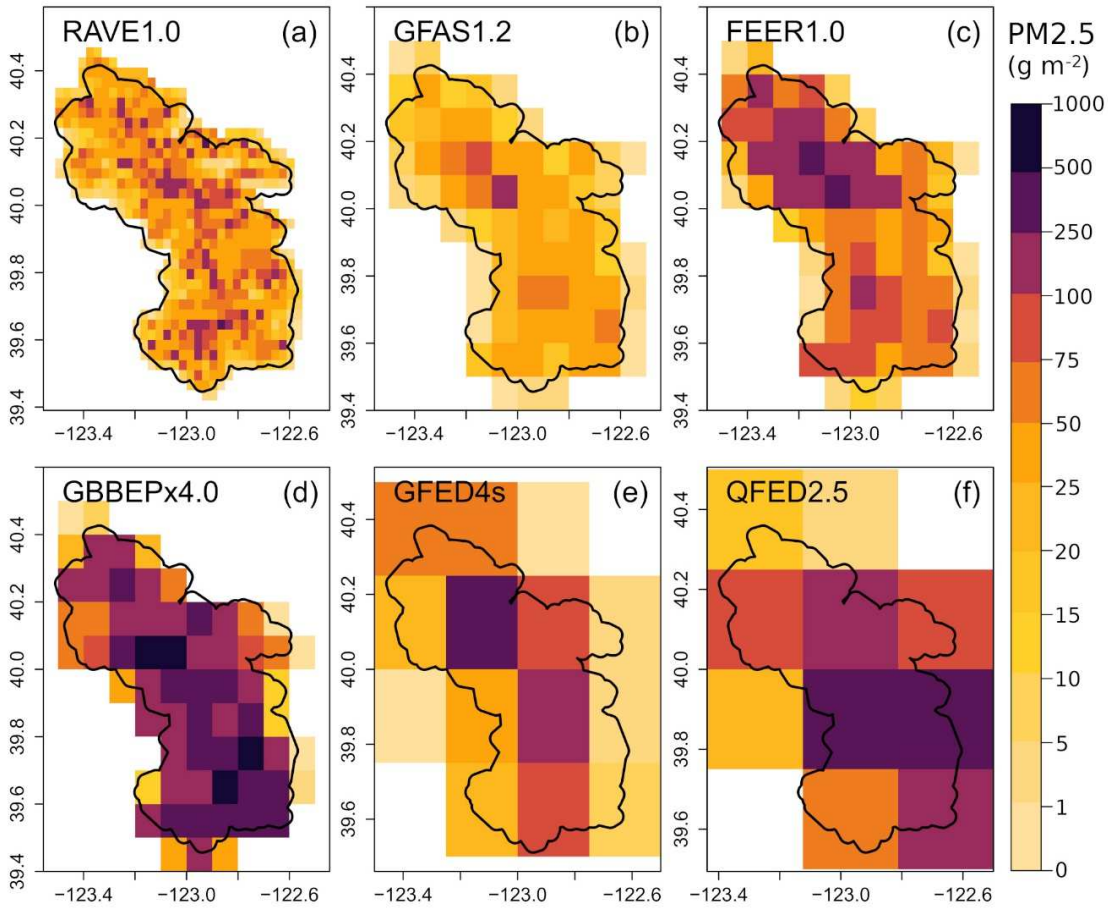

816

817 **Figure 13**. PM2.5 maps of California's largest August Complex Fire in 2020 from six emissions
818 datasets. (a) 3 km RAVE1.0, (b) 0.1 degree GFAS1.2, (c) 0.1° FEER1.0, (d) 0.1° GBBEPx4.0, (e)
819 0.25° GFED4s, and (f) 0.25° × 0.3125° QFED2.5. The black line is the buffered Landsat (30m)-
820 based fire perimeter outward by 3km.

821

822 **5. Discussion**

823 This study developed a robust algorithm to produce highest spatial and temporal
824 resolution biomass-burning emissions product, RAVE, across the CONUS by blending high-

825 temporal-resolution (5 minutes) ABI FRP and fine-spatial-resolution (375m) VIIRS FRP. It
826 significantly improves the quality of biomass burning emissions estimation.

827 5.1. Implications of High Spatiotemporal Resolution Emissions

828 Hourly fire emissions are one of the critical inputs for air quality forecast models. Almost
829 all the available fire emission inventories (e.g., Table 1) provide emissions at a daily basis or a
830 longer period. In the absence of hourly emission data, a fixed diurnal climatology is commonly
831 employed to redistribute daily emissions to 24 hours, which can lead to forecast errors (Bela et
832 al., 2022; O'Neill et al., 2021; Ye et al., 2021). For instance, the OC emissions predicted from 11
833 air quality forecast models with daily fire emissions as the input showed very different diurnal
834 patterns and peak occurrences from the ABI observations (Ye et al., 2021). The errors associated
835 with fixed diurnal cycles misrepresenting the dynamics in fire emissions has been shown in past
836 studies (Saide et al., 2015; Ye et al., 2021). Indeed, fire emissions are highly variable in seasonal
837 and diurnal patterns. This is evident in the time series of the hourly $PM_{2.5}$ emissions from three
838 California's largest wildfires in 2020 (Figure 9). In the three fires, hourly $PM_{2.5}$ shows very large
839 variations during intensive burning days (e.g., September 4-6 for the August Complex Fire,
840 Figure 9a), with variable peak hours. Moreover, nighttime emissions are also strong in these
841 forest fires. Evidently, a fixed emission diurnal cycle is inadequate to represent the large
842 variability of fire emissions. Especially, the commonly used Gaussian-shape diurnal curves
843 would likely misrepresent emission peaks and underestimate nighttime emissions substantially as
844 they have flat tails on both sides. As vegetation is increasingly flammable at night in the western
845 U.S. due to climate change (Balch et al., 2022; Freeborn et al., 2022), nocturnal fires and
846 emissions are more pronounced. Thus, our hourly RAVE emission data provide sources of fire

847 emissions (locations and amount) that are expected to improve air quality models for forecasting
848 smoke dispersion and transport across the CONUS.

849 High spatial-resolution emissions reflect fuel consumption. Most available emission
850 inventories provide estimates in 0.1 degree (~10 km) or coarser resolution grids (Table 1).
851 Emissions at high spatial resolution (e.g., 3km as in RAVE) improve the ability to track
852 emissions from individual fires, and reveal the heterogeneity of emissions in large wildfires
853 (Figures 7 and 13), which helps to understand the complexity of fuel consumption within a large
854 fire. This is very meaningful for fuel management and future fire activity and fire emissions
855 (Burke et al., 2021).

856

857 5.2. Accuracy of the RAVE Emissions

858 Validation and evaluation of biomass-burning emissions are crucial and remain
859 challenging tasks. Because of the wide availability of aerosol observations from ground-,
860 airborne-, and satellite-based instruments, these observed AOD values are widely used to
861 evaluate emissions estimates by comparing with the model-based AOD with the emissions
862 estimation as an input (Brown et al., 2021; Carter et al., 2020; Johnson et al., 2016; Kaiser et al.,
863 2012; Pan et al., 2020; Roberts et al., 2015; Ye et al., 2021; Zhang et al., 2014a). However, this
864 indirect evaluation is affected by uncertainties in AOD modeling because other parameters (e.g.,
865 plume injection, the depths of the planetary boundary layer (PBL), aerosol physical and chemical
866 properties, etc.) also play important roles (Curci et al., 2015; Das et al., 2017; Ye et al., 2021).
867 We directly evaluate the RAVE CO emissions using TROPOMI CO observations (Figure
868 11). The manually selected fires with fresh smoke plumes ensure the quality of samples (such as
869 cloud contamination and dilution) although the number of samples is relatively small. The

TROPOMI CO verified the reliability of emissions estimation in the RAVE, with a significant correlation (R^2=0.94, $p < 0.001$) and a difference less than 11%. The good agreement confirms the sound performance of the FRP-based emission estimation approach, which is consistent with our previous finding (Li et al., 2020b). This evaluation depends on the quality of TROPOMI CO in the selected samples, which is potentially affected by the background non-fire CO (e.g., biogenic sources) (Jiang et al., 2018b). By selecting background TROPOMI CO from the upwind and all-direction backgrounds, we found that the TROPOMI CO estimates are very similar (RMSE = 0.199, Figure 14; note that the RMSE is 0.043 if the fire with the largest CO is excluded.). This indicates the TROPOMI CO estimates are of high quality.

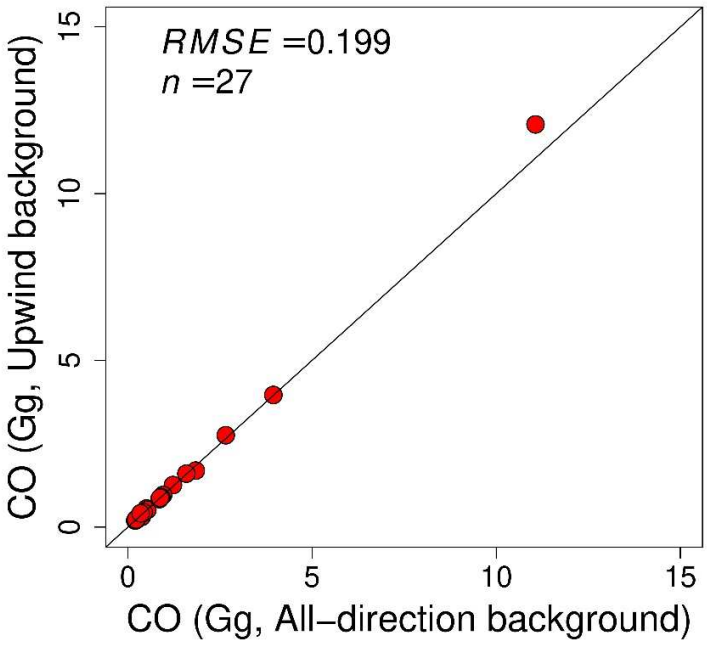

Figure 14. Comparison of the TROPOMI CO estimates based on the upwind and all-direction backgrounds over the selected 27 fires.

The TROPOMI CO based evaluation method has several advantages. First, CO is very suitable for tracking fire smoke emissions. Unlike aerosols in which masses change fast due to

884 evaporation, condensation, and the formation of secondary organic aerosols as smoke transports
885 and ages (Hodshire et al., 2019; Hodshire et al., 2021), CO is chemically inactive at the age of
886 smoke transportation (Hodshire et al., 2019; Yokelson et al., 2009). Moreover, the TROPOMI
887 CO data have very accurate CO column retrievals in clear skies and a spatial resolution to
888 capture a fire smoke plume in a single overpass (Borsdorff et al., 2018c). Second, TROPOMI
889 CO is directly calculated from fresh smoke plumes with negligible CO dilution, which has
890 advantages over the model-based approach that involves complex parameterizations. The
891 assumption of negligible CO dilution is reasonable because (1) the selected plumes are emitted
892 merely a few hours before the TROPOMI's overpass and (2) the evolution of a smoke plume
893 shape can be inspected using high temporal-resolution ABI true-color images. Third, the
894 TROPOMI CO can be applied easily to evaluate fire emissions in other fire-prone regions at
895 low-middle latitudes where high temporal-resolution FRP observations are available. Because of
896 the relatively coarse spatial resolution in TROPOMI (5.5km), it is difficult to apply this method
897 to evaluate emissions from very small fires. As a result, only one sample among the 27 selected
898 fires is selected for agriculture fires (Figure 11c).
899

900 5.3 Uncertainties in the RAVE Emissions

901 The reliable emission accuracy of the RAVE product is attributed mainly to the capability
902 of the combined fire observations from advanced sensors - ABI and VIIRS. By observing the
903 CONUS fires at an unprecedented temporal resolution of every five minutes, GOES-R series
904 ABI has the best-ever capability of depicting diurnal fire dynamics/evolutions that associate with
905 abrupt changes in fire weather, fuel characteristics, and topography (Schmidt et al., 2017).
906 Further, the fine-resolution VIIRS has significantly improved capabilities of observing small and

907 /or cool fires relative to legacy sensors (e.g., MODIS) and provides the highest spatial-resolution
908 FRP. Fusing FRP from both sensors guarantees accurate FRP diurnal cycles, and thereby reliable
909 FRE and emission estimates.

910 The RAVE emission estimates could contain some uncertainties that are associated with
911 parameters used to calculate biomass consumption and emissions. First, FRP diurnal cycle could
912 be unreliable in small fires, such as agricultural burnings, which usually have low intensity and
913 last a short period of minutes to a few hours. This makes it difficult to determine burning
914 duration and fill FRP gaps in the reconstruction of FRP diurnal cycles. Due to the lack of
915 ground-truth burning duration information, the assumption of one hour before and after a valid
916 FRP observation during FRP gap filling (c.f. Section 3.2.2) would underestimate FRE and
917 emissions if the actual burning duration is longer than two hours; otherwise, the assumption
918 would result in overestimation of FRE and emissions. Unfortunately, the accuracy of emissions
919 from small fires is hard to quantify using TROPOMI CO because of the relatively coarse spatial
920 resolution. Nevertheless, the RAVE $PM_{2.5}$ emissions for the CONUS agriculture fires are greatly
921 improved because of the fine spatial resolution VIIRS and high temporal resolution ABI
922 observations. The annual RAVE $PM_{2.5}$ estimates from agriculture fires are higher by a factor of
923 two than the mean annual total $PM_{2.5}$ emissions from 2011-2015, which were estimated from
924 1km MODIS FRP and 4km FRP from legacy GOES satellites (i.e., GOES-13 and GOES-15) (Li
925 et al., 2019). This indicates that RAVE captures many more small agriculture fires, because
926 agricultural fire emissions are relatively constant interannually across the CONUS (Li et al.,
927 2019; McCarty et al., 2009; Zhang et al., 2008).

928 Second, the obscuration of clouds and forest canopies could influence the RAVE
929 emissions estimation, but likely only to a limited extent because partial cloud contamination is

930 corrected and temporal gaps are filled. In the cloud-caused temporal gaps, the associated missing
931 FRP values were predicted using FRP diurnal climatologies and the fused ABI-VIIRS FRP (see
932 Section 3.2). Cloud correction was also applied to VIIRS FRP in grids that were partially
933 covered by clouds (see Section 3.1.1). Although it is difficult to evaluate the accuracy of cloud-
934 corrected FRP in the absence of ground-truth data, the proposed new cloud correction (Eq. (1)) is
935 able to account for potential FRP underestimation and avoid great FRP overestimation with a
936 large fraction of clouds in a grid. For example, as a cloud fraction grows from 50% to 90% in a
937 given grid, the corrected FRP increases by a factor of 0.7 – 2.3 using Eq. (1) but a factor of 1 – 9
938 based on the commonly used assumption that the burning conditions in clear areas and under
939 clouds are the same. The latter could result in the assumption of a large grid size fully burned.
940 This cloud-correction-caused overestimation issue has been pointed out in previous studies
941 (Darmenov et al., 2015; Giglio, 2007). Dense forest canopies attenuate fire-emitted radiative
942 energy (Roberts et al., 2018), which can reduce FRP retrievals by 15% in Africa (Roberts et al.,
943 2018). This amount of FRP underestimation could occur in the southeastern U.S. where surface
944 prescribed fires are common (Nowell et al., 2018). However, the canopy impact is likely much
945 smaller in forest fires in the western U.S. where forest fires are usually large and intense and
946 scorch tree canopies (Andela et al., 2019). In addition, we acknowledge that the omission of fires
947 could also cause underestimation of RAVE emissions because fires are very small or under
948 persistent heavy cloud cover.
949 Third, uncertainty in emission estimates could stem from biomass combustion coefficient
950 (F_c in Eq.6). We use a combustion coefficient (F_c) of 0.368 kg MJ^{-1} to convert FRE to dry matter
951 in the RAVE product. This value was reported initially in a small field fire experiment (Wooster
952 et al., 2005). Recent studies have further verified the usefulness of the coefficient: 0.298 kg MJ^{-1}

953 in prescribed fires with oak as the primary fuel (Kremens et al., 2012); 0.4 kg MJ^{-1} based on lab
954 experiment with western white pine needle as fuel when fuel moisture content is 10% (Smith et
955 al., 2013); 0.32 kg MJ^{-1} based on Landsat-based fuel consumption and FRP from MODIS and
956 legacy GOES at 445 wildfires across the CONUS (Li et al., 2018b); and 0.367 kg MJ^{-1} in two
957 wildfires with complex fuel types using the airborne Lidar-based fuel consumption and MODIS
958 FRP (McCarley et al., 2020). These studies indicate that the coefficient F_c varies within 18% of
959 the initial value 0.368 kg MJ^{-1}, which could result in some uncertainty in the emissions estimates.
960 Fourth, uncertainty in emission estimates could also arise from emission factor (EF_x in
961 Eq.7). Emission factors depend strongly on combustion phase that is typically a mixture of
962 smoldering and flaming phases (Christian et al., 2003; Liu et al., 2017; Prichard et al., 2020). As
963 combustion transits from smoldering to flaming phase, emission factor decreases for most of fire
964 emission species (e.g., CO_2, CO, and $PM_{2.5}$) but increases for a few species (e.g., NO_x and
965 sulfate), with a change by severalfold (Liu et al., 2017; Yokelson et al., 2007). Moreover,
966 emission factor also varies with fire types and fuel categories (Andreae, 2019; Liu et al., 2017;
967 Prichard et al., 2020). To account for various fires for a given species, emission factors for a
968 specific fuel (e.g., forest) are usually reported as the mean of available published values in many
969 regions (Akagi et al., 2011; Andreae, 2019; Prichard et al., 2020). As the RAVE emissions focus
970 on the CONUS, we used mean emission factors of reported values for fires in the temperate
971 North America, which were extracted from the recently compiled emission factor datasets
972 (Akagi et al., 2011; Andreae, 2019; Prichard et al., 2020). The influences of emission factors
973 could be potentially bypassed using emission coefficient that is a production of combustion
974 coefficient and emission factor (Ichoku and Ellison, 2014; Lu et al., 2019; Mota and Wooster,
975 2018). However, the emission coefficient is only available for a few species (e.g., total

976 particulate matter or TPM and CO) (Ichoku and Ellison, 2014; Lu et al., 2019; Mota and
977 Wooster, 2018), and it is very challenging to accurately determine.
978
979 5.4. Record-breaking Biomass-Burning Emissions in the 2020 Fire Season
980 Fire emissions in 2020 were record high across the CONUS. The fires scorched a total
981 area of 4 million ha (NIFC), which tops near 40-year fire records since 1980s. Accordingly, fires
982 consumed 221 Tg dry matter and emitted 2.25 Tg $PM_{2.5}$ (Table 1), which are approximately 2 - 3
983 folds higher than the annual mean biomass consumption (~41 - 57 Tg) and $PM_{2.5}$ emissions
984 (~0.72 Tg) of the past two decades (Li et al., 2019; Urbanski et al., 2018; Zhang et al., 2014b).
985 Moreover, the fire-emitted $PM_{2.5}$ emissions are as much as 75% of the annual $PM_{2.5}$ emissions
986 from all other non-fire sources (3 Tg) reported by the National Emissions Inventory (NEI,
987 https://www.epa.gov/air-emissions-inventories, last access on 16 February 2022) from the United
988 States Environmental Protection Agency (EPA).
989 In California, the 2020 wildfires emitted a total of 0.98 Tg $PM_{2.5}$ and 142 Tg CO_2, which
990 are larger by factors between 6.5 and 9 than the annual mean $PM_{2.5}$ (0.13 Tg) and CO_2 (14.3 Tg)
991 emissions during the past two decades, respectively (CARB, 2021). Moreover, the total
992 California wildfire $PM_{2.5}$ and CO_2 amounts are approximately 200-300% of the second-largest
993 emission year 2008, with 0.46 Tg $PM_{2.5}$ and 42 Tg CO_2 (CARB, 2021). In comparison with
994 emissions from other sources, the total CO_2 amount is also nearly one-third of the State-wide
995 CO_2-equivalent greenhouse gases (GHG) emissions in 2019 (418 Tg, the California Greenhouse
996 Gas Emission Inventory at https://ww2.arb.ca.gov/our-work/programs/ghg-inventory-program,
997 last access on 16 February 2022).

As a result, the enormous fire emissions strongly degrade air quality across west coast areas and mountain regions and influence public health (Li et al., 2021b), and challenge short-term GHG emissions goals (e.g., California's 2020 emissions limit in Forestry Sector, https://ww2.arb.ca.gov/ghg-inventory-data, last access on 16 February 2022). The record-high fire area and emissions are likely associated with several factors, including extreme fire weather, warming temperature, decreasing precipitation, and strong winds (Goss et al., 2020; Swain, 2021; Williams et al., 2019). Understanding the causes of the extreme nature of 2020 wildfires in California is not the focus of this study.

5.5. Sources of Discrepancies between RAVE and Other Inventories

Temporal and spatial scales matter to pinpoint emission discrepancies among different inventories. In the CONUS, the annual total $PM_{2.5}$ emissions from RAVE differ from QFED2.5 and GBBEPx4 by a factor of ~4 and the other inventories by a factor of less than 1.5 (Figure 12a). In the monthly scale, the largest discrepancy among different inventories in monthly total $PM_{2.5}$ on average is 16 (Figure 12b). Moreover, in California's 2020 top five largest fires, $PM_{2.5}$ emissions from eight inventories differ from each other by a factor of up to 18. The pattern of growing emissions discrepancy at finer spatiotemporal resolutions is also seen in other studies (Carter et al., 2020; Li et al., 2019; Liu et al., 2020; Pan et al., 2020). Thus, the large discrepancies at local scales offset each other after emissions being aggregated to regional or national scales.

The large discrepancies among fire emission inventories highlight the uncertainty in emission estimates. The emission discrepancy between inventories is associated with differences in biomass consumption estimates and emission factors. Recently, it has been found that

emission factor likely explains less than 30% of discrepancies among emission inventories while biomass consumption is the major driver of discrepancies in most global regions (Carter et al. 2020; Liu et al. 2020). Biomass consumption is estimated using FRP or burned area. Among five FRP-based inventories (Table 1), QFED2.5 and GBBEPx4 are higher by integer factors than the others, which is attributed mainly to the biome-specific scaling factors (1.8 - 4.5) for adjusting emissions (Darmenov and Silva, 2015; Zhang et al., 2019). The differences among RAVE1.0, GFAS1.2 and FEER1.0 are associated with differences in FRE calculation, combustion coefficient, smoke coefficient, and emission factor. GFAS estimates FRE by averaging daily MODIS FRP observations and integrating the mean FRP over 24 hours (Kaiser et al., 2012), and GFAS FRE is also used in FEER1.0 (Ichoku and Ellison, 2014). Due to limited daily MODIS observations, the MODIS FRP based FRE tends to be substantially overestimated in small fires because they usually burn for a short period (e.g., agriculture fires from 11 AM to 5 PM, Figure 8) and underestimated in large and intense fires when fires peak in other hours instead of MODIS daytime overpasses (Figures 5a & 9). Furthermore, relative to the constant combustion coefficient of 0.368 kg MJ^{-1} used in the RAVE, GFAS uses land cover specific coefficients that are 33% and 112% larger in temperate forest and savanna, respectively, but 21% smaller in cropland (Kaiser et al., 2012). FEER smoke coefficient can be affected by several factors (e.g., uncertainty in aerosol mass extinction efficiency, gaps in MODIS AOD observations, and the association of the mean TPM rate with MODIS FRP (Ichoku and Ellison, 2014).

Discrepancies between the burned area based emission inventories are also considerable (Figure 11 & Table 1), which are associated with the uncertainties in the conventional method. Among the burned area based inventories, WFEIS2.0 and GFED4s (for years before 2017) use MODIS burned area data. The large omission errors in MODIS burned area over small-sized

fires have been well known (Boschetti et al., 2019; Roteta et al., 2019), which is why GFED4s also includes separate burned areas for small fires (Randerson et al., 2012). FINN2.4 calculates burned area using MODIS and VIIRS I-band fire detections by assigning a fixed area to each detection (Wiedinmyer et al., 2011). Very simplified assumptions cause large uncertainty in burned area estimates because a fire detection algorithm can flag a fire pixel where 1000 K flaming fires burning an area of 0.0001 km^2 (Giglio et al., 2003). This likely explains why FINN2.4 burned area is higher than NIFC burned area and Landsat burned area by a factor of ~2.2 in the August Complex Fire. Further, uncertainties in fuel loadings and combustion completeness also influence the accuracy of emission estimates. For example, in the Creek Fire, FINN2.4 $PM_{2.5}$ is smaller than CARB $PM_{2.5}$ by a factor of two although FINN2.4 burned area is higher than the NIFC burned area by a factor of two. Obviously, the FINN2.4 $PM_{2.5}$ underestimation in the Creek Fire is attributed mainly to the differences in fuel loadings and combustion completeness. CARB uses the FCCS fuel loadings adjusted with fuel moisture while FINN uses literature-based statistic fuel loadings, which do not consider changes in fuel loadings due to a variety of factors, such as seasonal variation of fuel moisture, disturbances, vegetation regrowth, etc.

6. Conclusions

High spatiotemporal-resolution fire emission data are critical to air quality forecast models, yet they are very scarce among available emission inventories. We developed a new operational algorithm to generate regional hourly 3km fire emission product (namely RAVE) by fusing high temporal-resolution ABI FRP and fine spatial-resolution VIIRS FRP. Because of these new-generation sensors' advanced capabilities of fire observation, FRP diurnal cycles were

reconstructed to depict diurnal fire activities. We estimated one-year RAVE emissions for eight chemical species from April 2020 to March 2021 across the CONUS. The total $PM_{2.5}$ emissions in this study period are record-breaking high due to a large number of wildfires in the west coastal states, which are responsible for extremely unhealthy air quality and the burden of public health (Ford et al., 2018; Li et al., 2021b). The evaluation indicates that RAVE CO aligns well with TROPOMI CO, with a difference of 11% over 27 fire events. The good agreement verifies the good performance of the ABI-VIIRS FRP-based emissions estimation and reveals the reliable accuracy of the RAVE emissions. Compared with available global and regional fire emission inventories, RAVE shows similar values of the annual and national sum with some inventories, but differs very largely on the monthly scale and in individual fire events. This highlights the uncertainties in emission inventories and underscores the great need to improve emissions estimation using advanced algorithms and satellite observations. The hourly ABI-VIIRS FRP, demonstrated in this study, is promising in producing high-quality biomass burning emissions product (RAVE). As a result, the RAVE product is planned to be operational at NOAA and provides hourly emissions every six hours in near real-time for air quality forecast models.

Acknowledgments

This research was funded by the National Oceanic and Atmospheric Administration (NOAA) contract NA20OAR4600290. We thank NOAA, the European Space Agency (ESA), and the United States Geological Survey (USGS) for providing ABI and VIIRS active fire data, TROPOMI CO data, and Landsat burned area data. We thank NOAA/NESDIS/STAR Fire

Science Team members Wei Guo and Marina Tsidulko (I.M. Systems, Inc.) for providing persistent anomaly masks and selecting VIIRS I-band active fire data used in this study. We thank Zigang Wei (I.M. Systems, Inc.) for helping process TROPOMI CO data. We also thank all fire emission teams for making emissions inventories available to the public. We thank three reviewers' constructive comments that improved the original submission. The scientific results and conclusions, as well as any views or opinions expressed herein, are those of the author(s) and do not necessarily reflect those of NOAA or the Department of Commerce.

References

Akagi, S.K., Yokelson, R.J., Wiedinmyer, C., Alvarado, M.J., Reid, J.S., Karl, T., Crounse, J.D., & Wennberg, P.O. (2011). Emission factors for open and domestic biomass burning for use in atmospheric models. Atmos. Chem. Phys., 11, 4039-4072, https://doi.org/10.5194/acp-11-4039-2011.

Andela, N., Kaiser, J.W., van der Werf, G.R., & Wooster, M.J. (2015). New fire diurnal cycle characterizations to improve fire radiative energy assessments made from MODIS observations. Atmos. Chem. Phys., 15, 8831-8846, https://doi.org/10.5194/acp-15-8831-2015.

Andela, N., Morton, D.C., Giglio, L., Paugam, R., Chen, Y., Hantson, S., van der Werf, G.R., & Randerson, J.T. (2019). The Global Fire Atlas of individual fire size, duration, speed and direction. Earth Syst. Sci. Data, 11, 529-552, https://doi.org/10.5194/essd-11-529-2019.

Andreae, M.O. (2019). Emission of trace gases and aerosols from biomass burning – an updated assessment. Atmos. Chem. Phys., 19, 8523-8546, https://doi.org/10.5194/acp-19-8523-2019.

Appel, K.W., Napelenok, S.L., Foley, K.M., Pye, H.O.T., Hogrefe, C., Luecken, D.J., Bash, J.O., Roselle, S.J., Pleim, J.E., Foroutan, H., Hutzell, W.T., Pouliot, G.A., Sarwar, G., Fahey, K.M., Gantt, B., Gilliam, R.C., Heath, N.K., Kang, D., Mathur, R., Schwede, D.B., Spero, T.L., Wong, D.C., & Young, J.O. (2017). Description and evaluation of the Community Multiscale Air Quality (CMAQ) modeling system version 5.1. Geosci. Model Dev., 10, 1703-1732, https://doi.org/10.5194/gmd-10-1703-2017.

Archer-Nicholls, S., Lowe, D., Darbyshire, E., Morgan, W.T., Bela, M.M., Pereira, G., Trembath, J., Kaiser, J.W., Longo, K.M., Freitas, S.R., Coe, H., & McFiggans, G. (2015). Characterising Brazilian biomass burning emissions using WRF-Chem with MOSAIC sectional aerosol. Geosci. Model Dev., 8, 549-577, https://doi.org/10.5194/gmd-8-549-2015.

Balch, J.K., Abatzoglou, J.T., Joseph, M.B., Koontz, M.J., Mahood, A.L., McGlinchy, J., Cattau, M.E., & Williams, A.P. (2022). Warming weakens the night-time barrier to global fire. Nature, 602, 442-448, https://doi.org/10.1038/s41586-021-04325-1.

Bela, M.M., Kille, N., McKeen, S.A., Romero-Alvarez, J., Ahmadov, R., James, E., Pereira, G., Schmidt, C., Pierce, R.B., O'Neill, S.M., Zhang, X., Kondragunta, S., Wiedinmyer, C., & Volkamer, R. (2022). Quantifying Carbon Monoxide Emissions on the Scale of Large Wildfires. Geophysical Research Letters, 49, e2021GL095831, https://doi.org/10.1029/2021GL095831.

Bessho, K., Date, K., Hayashi, M., Ikeda, A., Imai, T., Inoue, H., Kumagai, Y., Miyakawa, T., Murata, H., Ohno, T., Okuyama, A., Oyama, R., Sasaki, Y., Shimazu, Y., Shimoji, K., Sumida, Y., Suzuki, M., Taniguchi, H., Tsuchiyama, H., Uesawa, D., Yokota, H., & Yoshida, R. (2016). An Introduction to Himawari-8/9 - Japan's New-Generation Geostationary Meteorological Satellites. Journal of the Meteorological Society of Japan. Ser. II, 94, 151-183. https://doi.org/10.2151/jmsj.2016-009.

Bond, T.C., Doherty, S.J., Fahey, D.W., Forster, P.M., Berntsen, T., DeAngelo, B.J., Flanner, M.G., Ghan, S., Kärcher, B., Koch, D., Kinne, S., Kondo, Y., Quinn, P.K., Sarofim, M.C., Schultz, M.G., Schulz, M., Venkataraman, C., Zhang, H., Zhang, S., Bellouin, N., Guttikunda, S.K., Hopke, P.K., Jacobson, M.Z., Kaiser, J.W., Klimont, Z., Lohmann, U., Schwarz, J.P., Shindell, D., Storelvmo, T., Warren, S.G., & Zender, C.S. (2013). Bounding the role of black carbon in the climate system: A scientific assessment. Journal of Geophysical Research: Atmospheres, 118, 5380-5552, https://doi.org/10.1002/jgrd.50171.

Boschetti, L., Roy, D.P., Giglio, L., Huang, H., Zubkova, M., & Humber, M.L. (2019). Global validation of the collection 6 MODIS burned area product. Remote Sensing of Environment, 235, 111490, https://doi.org/10.1016/j.rse.2019.111490.

Brown, H., Liu, X., Pokhrel, R., Murphy, S., Lu, Z., Saleh, R., Mielonen, T., Kokkola, H., Bergman, T., Myhre, G., Skeie, R.B., Watson-Paris, D., Stier, P., Johnson, B., Bellouin, N., Schulz, M., Vakkari, V., Beukes, J.P., van

Zyl, P.G., Liu, S., & Chand, D. (2021). Biomass burning aerosols in most climate models are too absorbing. Nature Communications, 12, 277, https://doi.org/10.1038/s41467-020-20482-9.

Burke, M., Driscoll, A., Heft-Neal, S., Xue, J., Burney, J., & Wara, M. (2021). The changing risk and burden of wildfire in the United States. Proceedings of the National Academy of Sciences, 118, e2011048118, https://doi.org/10.1073/pnas.2011048118.

Campbell, J., Donato, D., Azuma, D., & Law, B. (2007). Pyrogenic carbon emission from a large wildfire in Oregon, United States. Journal of Geophysical Research: Biogeosciences, 112, G04014, https://doi.org/10.1029/2007JG000451.

Cao, C., Luccia, F.J.D., Xiong, X., Wolfe, R., & Weng, F. (2014). Early On-Orbit Performance of the Visible Infrared Imaging Radiometer Suite Onboard the Suomi National Polar-Orbiting Partnership (S-NPP) Satellite. Ieee Transactions on Geoscience and Remote Sensing, 52, 1142-1156, https://doi.org/10.1109/TGRS.2013.2247768.

CARB (2021). California Wildfire Emission Estimates. Available at: https://ww2.arb.ca.gov/wildfire-emissions, last access on 12/1/2021.

Carter, T.S., Heald, C.L., Jimenez, J.L., Campuzano-Jost, P., Kondo, Y., Moteki, N., Schwarz, J.P., Wiedinmyer, C., Darmenov, A.S., da Silva, A.M., & Kaiser, J.W. (2020). How emissions uncertainty influences the distribution and radiative impacts of smoke from fires in North America. Atmos. Chem. Phys., 20, 2073-2097, https://doi.org/10.5194/acp-20-2073-2020.

Christian, T.J., Kleiss, B., Yokelson, R.J., Holzinger, R., Crutzen, P.J., Hao, W.M., Saharjo, B.H., & Ward, D.E. (2003). Comprehensive laboratory measurements of biomass-burning emissions: 1. Emissions from Indonesian, African, and other fuels. Journal of Geophysical Research: Atmospheres, 108, https://doi.org/10.1029/2003JD003704.

Chuvieco, E., Aguado, I., Salas, J., García, M., Yebra, M., & Oliva, P. (2020). Satellite Remote Sensing Contributions to Wildland Fire Science and Management. Current Forestry Reports, 6, 81-96. https://doi.org/10.1007/s40725-020-00116-5.

Crutzen, P.J., & Andreae, M.O. (1990). Biomass Burning in the Tropics: Impact on Atmospheric Chemistry and Biogeochemical Cycles. Science, 250, 1669-1678, https://doi.org/10.1126/science.250.4988.1669.

1168 Csiszar, I., Schroeder, W., Giglio, L., Ellicott, E., Vadrevu, K.P., Justice, C.O., & Wind, B. (2014). Active fires from
1169 the Suomi NPP Visible Infrared Imaging Radiometer Suite: Product status and first evaluation results. Journal
1170 of Geophysical Research: Atmospheres, 119, 2013JD020453, https://doi.org/10.1002/2013JD020453.
1171 Curci, G., Hogrefe, C., Bianconi, R., Im, U., Balzarini, A., Baró, R., Brunner, D., Forkel, R., Giordano, L., Hirtl, M.,
1172 Honzak, L., Jiménez-Guerrero, P., Knote, C., Langer, M., Makar, P.A., Pirovano, G., Pérez, J.L., San José, R.,
1173 Syrakov, D., Tuccella, P., Werhahn, J., Wolke, R., Žabkar, R., Zhang, J., & Galmarini, S. (2015). Uncertainties
1174 of simulated aerosol optical properties induced by assumptions on aerosol physical and chemical properties: An
1175 AQMEII-2 perspective. Atmospheric Environment, 115, 541-552,
1176 https://doi.org/10.1016/j.atmosenv.2014.09.009.
1177 Darmenov, A.S., & Silva, A.d. (2015). The Quick Fire Emissions Dataset (QFED): Documentation of versions 2.1,
1178 2.2 and 2.4. In R.D. Koster (Ed.), Technical Report Series on Global Modeling and Data Assimilation (p. 212):
1179 NASA
1180 Das, S., Harshvardhan, H., Bian, H., Chin, M., Curci, G., Protonotariou, A.P., Mielonen, T., Zhang, K., Wang, H., &
1181 Liu, X. (2017). Biomass burning aerosol transport and vertical distribution over the South African-Atlantic
1182 region. Journal of Geophysical Research: Atmospheres, 122, 6391-6415, https://doi.org/10.1002/2016jd026421.
1183 Di Giuseppe, F., Benedetti, A., Coughlan, R., Vitolo, C., & Vuckovic, M. (2021). A Global Bottom-Up Approach to
1184 Estimate Fuel Consumed by Fires Using Above Ground Biomass Observations. Geophysical Research Letters,
1185 48, e2021GL095452. https://doi.org/10.1029/2021GL095452.
1186 Duncan, B.N., Logan, J.A., Bey, I., Megretskaia, I.A., Yantosca, R.M., Novelli, P.C., Jones, N.B., & Rinsland, C.P.
1187 (2007). Global budget of CO, 1988–1997: Source estimates and validation with a global model. Journal of
1188 Geophysical Research: Atmospheres, 112, https://doi.org/10.1029/2007jd008459.
1189 Ford, B., Val Martin, M., Zelasky, S.E., Fischer, E.V., Anenberg, S.C., Heald, C.L., & Pierce, J.R. (2018). Future
1190 Fire Impacts on Smoke Concentrations, Visibility, and Health in the Contiguous United States. GeoHealth, 0,
1191 https://doi.org/10.1029/2018GH000144.
1192 Freeborn, P.H., Jolly, W.M., Cochrane, M.A., & Roberts, G. (2022). Large wildfire driven increases in nighttime
1193 fire activity observed across CONUS from 2003–2020. Remote Sensing of Environment, 268, 112777,
1194 https://doi.org/10.1016/j.rse.2021.112777.

1195 Freeborn, P.H., Wooster, M.J., Hao, W.M., Ryan, C.A., Nordgren, B.L., Baker, S.P., & Ichoku, C. (2008).
1196 Relationships between energy release, fuel mass loss, and trace gas and aerosol emissions during laboratory
1197 biomass fires. Journal of Geophysical Research-Atmospheres, 113, D01301,
1198 https://doi.org/10.1029/2007jd008679.
1199 Freeborn, P.H., Wooster, M.J., Roberts, G., Malamud, B.D., & Xu, W. (2009). Development of a virtual active fire
1200 product for Africa through a synthesis of geostationary and polar orbiting satellite data. Remote Sensing of
1201 Environment, 113, 1700-1711, https://doi.org/10.1016/j.rse.2009.03.013.
1202 French, N.H.F., de Groot, W.J., Jenkins, L.K., Rogers, B.M., Alvarado, E., Amiro, B., de Jong, B., Goetz, S., Hoy,
1203 E., Hyer, E., Keane, R., Law, B.E., McKenzie, D., McNulty, S.G., Ottmar, R., Pérez-Salicrup, D.R., Randerson,
1204 J., Robertson, K.M., & Turetsky, M. (2011). Model comparisons for estimating carbon emissions from North
1205 American wildland fire. Journal of Geophysical Research: Biogeosciences, 116, G00K05,
1206 https://doi.org/10.1029/2010JG001469.
1207 French, N.H.F., McKenzie, D., Erickson, T., Koziol, B., Billmire, M., Endsley, K.A., Scheinerman, N.K.Y., Jenkins,
1208 L., Miller, M.E., Ottmar, R., & Prichard, S. (2014). Modeling Regional-Scale Wildland Fire Emissions with the
1209 Wildland Fire Emissions Information System. Earth Interactions, 18, 1-26, https://doi.org/10.1175/EI-D-14-
1210 0002.1.
1211 Friedl, M.A., Sulla-Menashe, D., Tan, B., Schneider, A., Ramankutty, N., Sibley, A., & Huang, X. (2010). MODIS
1212 Collection 5 global land cover: Algorithm refinements and characterization of new datasets. Remote Sensing of
1213 Environment, 114, 168-182, https://doi.org/10.1016/j.rse.2009.08.016.
1214 Friedlingstein, P., O'Sullivan, M., Jones, M.W., Andrew, R.M., Hauck, J., Olsen, A., Peters, G.P., Peters, W.,
1215 Pongratz, J., Sitch, S., Le Quéré, C., Canadell, J.G., Ciais, P., Jackson, R.B., Alin, S., Aragão, L.E.O.C., Arneth,
1216 A., Arora, V., Bates, N.R., Becker, M., Benoit-Cattin, A., Bittig, H.C., Bopp, L., Bultan, S., Chandra, N.,
1217 Chevallier, F., Chini, L.P., Evans, W., Florentie, L., Forster, P.M., Gasser, T., Gehlen, M., Gilfillan, D.,
1218 Gkritzalis, T., Gregor, L., Gruber, N., Harris, I., Hartung, K., Haverd, V., Houghton, R.A., Ilyina, T., Jain, A.K.,
1219 Joetzjer, E., Kadono, K., Kato, E., Kitidis, V., Korsbakken, J.I., Landschützer, P., Lefèvre, N., Lenton, A.,
1220 Lienert, S., Liu, Z., Lombardozzi, D., Marland, G., Metzl, N., Munro, D.R., Nabel, J.E.M.S., Nakaoka, S.I.,
1221 Niwa, Y., O'Brien, K., Ono, T., Palmer, P.I., Pierrot, D., Poulter, B., Resplandy, L., Robertson, E., Rödenbeck,
1222 C., Schwinger, J., Séférian, R., Skjelvan, I., Smith, A.J.P., Sutton, A.J., Tanhua, T., Tans, P.P., Tian, H.,

Tilbrook, B., van der Werf, G., Vuichard, N., Walker, A.P., Wanninkhof, R., Watson, A.J., Willis, D., Wiltshire, A.J., Yuan, W., Yue, X., & Zaehle, S. (2020). Global Carbon Budget 2020. Earth Syst. Sci. Data, 12, 3269-3340, https://doi.org/10.5194/essd-12-3269-2020.

Fu, Y., Li, R., Wang, X., Bergeron, Y., Valeria, O., Chavardès, R.D., Wang, Y., & Hu, J. (2020). Fire Detection and Fire Radiative Power in Forests and Low-Biomass Lands in Northeast Asia: MODIS versus VIIRS Fire Products. Remote Sensing, 12, 2870, https://doi.org/10.3390/rs12182870.

Giglio, L. (2007). Characterization of the tropical diurnal fire cycle using VIRS and MODIS observations. Remote Sensing of Environment, 108, 407-421, https://doi.org/10.1016/j.rse.2006.11.018.

Giglio, L., Descloitres, J., Justice, C.O., & Kaufman, Y.J. (2003). An Enhanced Contextual Fire Detection Algorithm for MODIS. Remote Sensing of Environment, 87, 273-282, https://doi.org/10.1016/S0034-4257(03)00184-6.

Giglio, L., Schroeder, W., & Justice, C.O. (2016). The collection 6 MODIS active fire detection algorithm and fire products. Remote Sensing of Environment, 178, 31-41, https://doi.org/10.1016/j.rse.2016.02.054.

Goss, M., Swain, D.L., Abatzoglou, J.T., Sarhadi, A., Kolden, C.A., Williams, A.P., & Diffenbaugh, N.S. (2020). Climate change is increasing the likelihood of extreme autumn wildfire conditions across California. Environmental Research Letters, 15, 094016, https://doi.org/10.1088/1748-9326/ab83a7.

Hao, W.M., Liu, M.-H., & Crutzen, P.J. (1990). Estimates of Annual and Regional Releases of CO2 and Other Trace Gases to the Atmosphere from Fires in the Tropics, Based on the FAO Statistics for the Period 1975–1980. In J.G. Goldammer (Ed.), Fire in the Tropical Biota: Ecosystem Processes and Global Challenges (pp. 440-462). Berlin, Heidelberg: Springer Berlin Heidelberg

Hawbaker, T.J., Vanderhoof, M.K., Schmidt, G.L., Beal, Y.-J., Picotte, J.J., Takacs, J.D., Falgout, J.T., & Dwyer, J.L. (2020). The Landsat Burned Area algorithm and products for the conterminous United States. Remote Sensing of Environment, 244, 111801, https://doi.org/10.1016/j.rse.2020.111801.

Hély, C., Alleaume, S., Swap, R.J., Shugart, H., H., & Justice, C.O. (2003). SAFARI-2000 characterization of fuels, fire behavior, combustion completeness, and emissions from experimental burns in infertile grass savannas in western Zambia. Journal of Arid Environments, 54, 381-394, http://dx.doi.org/10.1006/jare.2002.1097.

Hodshire, A.L., Bian, Q., Ramnarine, E., Lonsdale, C.R., Alvarado, M.J., Kreidenweis, S.M., Jathar, S.H., & Pierce, J.R. (2019). More Than Emissions and Chemistry: Fire Size, Dilution, and Background Aerosol Also Greatly

Influence Near-Field Biomass Burning Aerosol Aging. Journal of Geophysical Research: Atmospheres, 124, 5589-5611, https://doi.org/10.1029/2018JD029674.

Hodshire, A.L., Ramnarine, E., Akherati, A., Alvarado, M.L., Farmer, D.K., Jathar, S.H., Kreidenweis, S.M., Lonsdale, C.R., Onasch, T.B., Springston, S.R., Wang, J., Wang, Y., Kleinman, L.I., Sedlacek Iii, A.J., & Pierce, J.R. (2021). Dilution impacts on smoke aging: evidence in Biomass Burning Observation Project (BBOP) data. Atmos. Chem. Phys., 21, 6839-6855, https://doi.org/10.5194/acp-21-6839-2021.

Holmlund, K., Grandell, J., Schmetz, J., Stuhlmann, R., Bojkov, B., Munro, R., Lekouara, M., Coppens, D., Viticchie, B., August, T., Theodore, B., Watts, P., Dobber, M., Fowler, G., Bojinski, S., Schmid, A., Salonen, K., Tjemkes, S., Aminou, D., & Blythe, P. (2021). Meteosat Third Generation (MTG): Continuation and Innovation of Observations from Geostationary Orbit. Bulletin of the American Meteorological Society, 102, E990-E1015. 10.1175/BAMS-D-19-0304.1.

Huang, R., Zhang, X., Chan, D., Kondragunta, S., Russell Armistead, G., & Odman, M.T. (2018). Burned Area Comparisons Between Prescribed Burning Permits in Southeastern United States and Two Satellite‐Derived Products. Journal of Geophysical Research: Atmospheres, 123, 4746-4757, https://doi.org/10.1029/2017JD028217.

Ichoku, C., & Ellison, L. (2014). Global top-down smoke-aerosol emissions estimation using satellite fire radiative power measurements. Atmos. Chem. Phys., 14, 6643-6667, 10.5194/acp-14-6643-2014.

Ichoku, C., Martins, J.V., Kaufman, Y.J., Wooster, M.J., Freeborn, P.H., Hao, W.M., Baker, S., Ryan, C.A., & Nordgren, B.L. (2008). Laboratory investigation of fire radiative energy and smoke aerosol emissions. Journal of Geophysical Research: Atmospheres, 113, https://doi.org/10.1029/2007jd009659.

Inness, A., Ades, M., Agustí-Panareda, A., Barré, J., Benedictow, A., Blechschmidt, A.M., Dominguez, J.J., Engelen, R., Eskes, H., Flemming, J., Huijnen, V., Jones, L., Kipling, Z., Massart, S., Parrington, M., Peuch, V.H., Razinger, M., Remy, S., Schulz, M., & Suttie, M. (2019). The CAMS reanalysis of atmospheric composition. Atmos. Chem. Phys., 19, 3515-3556, https://doi.org/10.5194/acp-19-3515-2019.

IPCC (2021). The Sixth Assessment Report, Climate Change 2021: The Physical Science Basis. In (pp. 1-3494)

Jacobson, M.Z. (2014). Effects of biomass burning on climate, accounting for heat and moisture fluxes, black and brown carbon, and cloud absorption effects. Journal of Geophysical Research: Atmospheres, 119, 2014JD021861, https://doi.org/10.1002/2014JD021861.

Jaffe, D.A., O'Neill, S.M., Larkin, N.K., Holder, A.L., Peterson, D.L., Halofsky, J.E., & Rappold, A.G. (2020). Wildfire and prescribed burning impacts on air quality in the United States. Journal of the Air & Waste Management Association, null-null, https://doi.org/10.1080/10962247.2020.1749731.

Jiang, Z., Jones, D.B.A., Kopacz, M., Liu, J., Henze, D.K., & Heald, C. (2011). Quantifying the impact of model errors on top-down estimates of carbon monoxide emissions using satellite observations. Journal of Geophysical Research: Atmospheres, 116, https://doi.org/10.1029/2010jd015282.

Jiang, Z., Jones, D.B.A., Worden, H.M., Deeter, M.N., Henze, D.K., Worden, J., Bowman, K.W., Brenninkmeijer, C.A.M., & Schuck, T.J. (2013). Impact of model errors in convective transport on CO source estimates inferred from MOPITT CO retrievals. Journal of Geophysical Research: Atmospheres, 118, 2073-2083, https://doi.org/10.1002/jgrd.50216.

Jiang, Z., McDonald, B.C., Worden, H., Worden, J.R., Miyazaki, K., Qu, Z., Henze, D.K., Jones, D.B.A., Arellano, A.F., Fischer, E.V., Zhu, L., & Boersma, K.F. (2018). Unexpected slowdown of US pollutant emission reduction in the past decade. Proceedings of the National Academy of Sciences, 115, 5099-5104, https://doi.org/10.1073/pnas.1801191115.

Jiang, Z., Worden, J.R., Worden, H., Deeter, M., Jones, D.B.A., Arellano, A.F., & Henze, D.K. (2017). A 15-year record of CO emissions constrained by MOPITT CO observations. Atmos. Chem. Phys., 17, 4565-4583, https://doi.org/10.5194/acp-17-4565-2017.

Jin, X., Zhu, Q., & Cohen, R.C. (2021). Direct estimates of biomass burning NOx emissions and lifetimes using daily observations from TROPOMI. Atmos. Chem. Phys., 21, 15569-15587, https://doi.org/10.5194/acp-21-15569-2021.

Johnson, B.T., Haywood, J.M., Langridge, J.M., Darbyshire, E., Morgan, W.T., Szpek, K., Brooke, J.K., Marenco, F., Coe, H., Artaxo, P., Longo, K.M., Mulcahy, J.P., Mann, G.W., Dalvi, M., & Bellouin, N. (2016). Evaluation of biomass burning aerosols in the HadGEM3 climate model with observations from the SAMBBA field campaign. Atmos. Chem. Phys., 16, 14657-14685, https://doi.org/10.5194/acp-16-14657-2016.

Johnston, F.H., Henderson, S.B., Chen, Y., Randerson, J.T., Marlier, M., DeFries, R.S., Kinney, P., Bowman, D.M., & Brauer, M. (2012). Estimated global mortality attributable to smoke from landscape fires. Environmental Health Perspectives, 120, https://doi.org/10.1289/ehp.1104422.

1306 Kaiser, J.W., Heil, A., Andreae, M.O., Benedetti, A., Chubarova, N., Jones, L., Morcrette, J.J., Razinger, M.,
1307 Schultz, M.G., Suttie, M., & van der Werf, G.R. (2012). Biomass burning emissions estimated with a global fire
1308 assimilation system based on observed fire radiative power. Biogeosciences, 9, 527-554,
1309 https://doi.org/10.5194/bg-9-527-2012.
1310 Kaufman, Y.J., Kleidman, R.G., & King, M.D. (1998). SCAR-B fires in the tropics: Properties and remote sensing
1311 from EOS-MODIS. Journal of Geophysical Research: Atmospheres, 103, 31955-31968, 10.1029/98JD02460.
1312 Kaufman, Y.J., Koren, I., Remer, L.A., Rosenfeld, D., & Rudich, Y. (2005). The effect of smoke, dust, and pollution
1313 aerosol on shallow cloud development over the Atlantic Ocean. Proceedings of the National Academy of
1314 Sciences of the United States of America, 102, 11207-11212, https://doi.org/10.1073/pnas.0505191102.
1315 Keane, R.E. (2013). Describing wildland surface fuel loading for fire management: a review of approaches, methods
1316 and systems. International Journal of Wildland Fire, 22, 51-62, https://doi.org/10.1071/WF11139.
1317 Konovalov, I.B., Berezin, E.V., Ciais, P., Broquet, G., Beekmann, M., Hadji-Lazaro, J., Clerbaux, C., Andreae,
1318 M.O., Kaiser, J.W., & Schulze, E.D. (2014). Constraining CO2 emissions from open biomass burning by
1319 satellite observations of co-emitted species: a method and its application to wildfires in Siberia. Atmos. Chem.
1320 Phys., 14, 10383-10410, https://doi.org/10.5194/acp-14-10383-2014.
1321 Kopacz, M., Jacob, D.J., Fisher, J.A., Logan, J.A., Zhang, L., Megretskaia, I.A., Yantosca, R.M., Singh, K., Henze,
1322 D.K., Burrows, J.P., Buchwitz, M., Khlystova, I., McMillan, W.W., Gille, J.C., Edwards, D.P., Eldering, A.,
1323 Thouret, V., & Nedelec, P. (2010). Global estimates of CO sources with high resolution by adjoint inversion of
1324 multiple satellite datasets (MOPITT, AIRS, SCIAMACHY, TES). Atmos. Chem. Phys., 10, 855-876,
1325 https://doi.org/10.5194/acp-10-855-2010.
1326 Kremens, R.L., Dickinson, M.B., & Bova, A.S. (2012). Radiant flux density, energy density and fuel consumption in
1327 mixed-oak forest surface fires. International Journal of Wildland Fire, 21, 722-730,
1328 https://doi.org/10.1071/WF10143.
1329 Kumar, S.S., Roy, D.P., Boschetti, L., & Kremens, R. (2011). Exploiting the power law distribution properties of
1330 satellite fire radiative power retrievals: A method to estimate fire radiative energy and biomass burned from
1331 sparse satellite observations. Journal of Geophysical Research: Atmospheres, 116, D19303,
1332 https://doi.org/10.1029/2011JD015676.

1333 Li, F., Zhang, X., & Kondragunta, S. (2020a). Biomass Burning in Africa: An Investigation of Fire Radiative Power
1334 Missed by MODIS Using the 375 m VIIRS Active Fire Product. Remote Sensing, 12, 1561,
1335 https://doi.org/10.3390/rs12101561.
1336 Li, F., Zhang, X., & Kondragunta, S. (2021a). Highly anomalous fire emissions from the 2019–2020 Australian
1337 bushfires. Environmental Research Communications, https://doi.org/10.1088/2515-7620/ac2e6f.
1338 Li, F., Zhang, X., Kondragunta, S., & Csiszar, I. (2018a). Comparison of Fire Radiative Power Estimates From
1339 VIIRS and MODIS Observations. Journal of Geophysical Research: Atmospheres, 123, 4545-4563,
1340 https://doi.org/10.1029/2017JD027823.
1341 Li, F., Zhang, X., Kondragunta, S., & Lu, X. (2020b). An evaluation of advanced baseline imager fire radiative
1342 power based wildfire emissions using carbon monoxide observed by the Tropospheric Monitoring Instrument
1343 across the conterminous United States. Environmental Research Letters, 15, 094049,
1344 https://doi.org/10.1088/1748-9326/ab9d3a.
1345 Li, F., Zhang, X., Kondragunta, S., & Roy, D.P. (2018b). Investigation of the Fire Radiative Energy Biomass
1346 Combustion Coefficient: A Comparison of Polar and Geostationary Satellite Retrievals Over the Conterminous
1347 United States. Journal of Geophysical Research: Biogeosciences, 123, 722-739,
1348 https://doi.org/10.1002/2017JG004279.
1349 Li, F., Zhang, X., Kondragunta, S., Schmidt, C.C., & Holmes, C.D. (2020c). A preliminary evaluation of GOES-16
1350 active fire product using Landsat-8 and VIIRS active fire data, and ground-based prescribed fire records.
1351 Remote Sensing of Environment, 237, 111600, https://doi.org/10.1016/j.rse.2019.111600.
1352 Li, F., Zhang, X., Roy, D.P., & Kondragunta, S. (2019). Estimation of biomass-burning emissions by fusing the fire
1353 radiative power retrievals from polar-orbiting and geostationary satellites across the conterminous United States.
1354 Atmospheric Environment, 211, 274-287, https://doi.org/10.1016/j.atmosenv.2019.05.017.
1355 Li, Y., Tong, D., Ma, S., Zhang, X., Kundragunta, S., Li, F., & Saylor, R. (2021b). Dominance of Wildfires Impact
1356 on Air Quality Exceedances during the 2020 Record‐Breaking Wildfire Season in the United States.
1357 Geophysical Research Letters, e2021GL094908, https://doi.org/10.1029/2021GL094908.
1358 Liu, M., Song, Y., Yao, H., Kang, Y., Li, M., Huang, X., & Hu, M. (2015). Estimating emissions from agricultural
1359 fires in the North China Plain based on MODIS fire radiative power. Atmospheric Environment, 112, 326-334,
1360 https://doi.org/10.1016/j.atmosenv.2015.04.058.

Liu, T., Marlier, M.E., Karambelas, A., Jain, M., Singh, S., Singh, M.K., Gautam, R., & DeFries, R.S. (2019). Missing emissions from post-monsoon agricultural fires in northwestern India: regional limitations of MODIS burned area and active fire products. Environmental Research Communications, 1, 011007, https://doi.org/10.1088/2515-7620/ab056c.

Liu, T., Mickley, L.J., Marlier, M.E., DeFries, R.S., Khan, M.F., Latif, M.T., & Karambelas, A. (2020). Diagnosing spatial biases and uncertainties in global fire emissions inventories: Indonesia as regional case study. Remote Sensing of Environment, 237, 111557, https://doi.org/10.1016/j.rse.2019.111557.

Liu, X., Huey, L.G., Yokelson, R.J., Selimovic, V., Simpson, I.J., Müller, M., Jimenez, J.L., Campuzano-Jost, P., Beyersdorf, A.J., Blake, D.R., Butterfield, Z., Choi, Y., Crounse, J.D., Day, D.A., Diskin, G.S., Dubey, M.K., Fortner, E., Hanisco, T.F., Hu, W., King, L.E., Kleinman, L., Meinardi, S., Mikoviny, T., Onasch, T.B., Palm, B.B., Peischl, J., Pollack, I.B., Ryerson, T.B., Sachse, G.W., Sedlacek, A.J., Shilling, J.E., Springston, S., St. Clair, J.M., Tanner, D.J., Teng, A.P., Wennberg, P.O., Wisthaler, A., & Wolfe, G.M. (2017). Airborne measurements of western U.S. wildfire emissions: Comparison with prescribed burning and air quality implications. Journal of Geophysical Research: Atmospheres, 122, 6108-6129, https://doi.org/10.1016/10.1002/2016JD026315.

Liu, X., Zhang, Y., Huey, L.G., Yokelson, R.J., Wang, Y., Jimenez, J.L., Campuzano-Jost, P., Beyersdorf, A.J., Blake, D.R., Choi, Y., St. Clair, J.M., Crounse, J.D., Day, D.A., Diskin, G.S., Fried, A., Hall, S.R., Hanisco, T.F., King, L.E., Meinardi, S., Mikoviny, T., Palm, B.B., Peischl, J., Perring, A.E., Pollack, I.B., Ryerson, T.B., Sachse, G., Schwarz, J.P., Simpson, I.J., Tanner, D.J., Thornhill, K.L., Ullmann, K., Weber, R.J., Wennberg, P.O., Wisthaler, A., Wolfe, G.M., & Ziemba, L.D. (2016). Agricultural fires in the southeastern U.S. during SEAC4RS: Emissions of trace gases and particles and evolution of ozone, reactive nitrogen, and organic aerosol. Journal of Geophysical Research: Atmospheres, 121, 2016JD025040, https://doi.org/10.1016/10.1002/2016JD025040.

Lu, X., Zhang, X., Li, F., & Cochrane, M.A. (2019). Investigating Smoke Aerosol Emission Coefficients using MODIS Active Fire and Aerosol Products — A Case Study in the CONUS and Indonesia. Journal of Geophysical Research: Biogeosciences, 0, https://doi.org/10.1016/10.1029/2018jg004974.

Lu, X., Zhang, X., Li, F., Gao, L., Graham, L., Vetrita, Y., Saharjo, B.H., & Cochrane, M.A. (2021). Drainage canal impacts on smoke aerosol emissions for Indonesian peatland and non-peatland fires. Environmental Research Letters, https://doi.org/10.1016/10.1088/1748-9326/ac2011.

McCarley, T.R., Hudak, A.T., Sparks, A.M., Vaillant, N.M., Meddens, A.J.H., Trader, L., Mauro, F., Kreitler, J., & Boschetti, L. (2020). Estimating wildfire fuel consumption with multitemporal airborne laser scanning data and demonstrating linkage with MODIS-derived fire radiative energy. Remote Sensing of Environment, 251, 112114, https://doi.org/10.1016/j.rse.2020.112114.

McCarty, J.L., Korontzi, S., Justice, C.O., & Loboda, T. (2009). The spatial and temporal distribution of crop residue burning in the contiguous United States. Science of The Total Environment, 407, 5701-5712, https://doi.org/10.1016/10.1016/j.scitotenv.2009.07.009.

Mota, B., & Wooster, M.J. (2018). A new top-down approach for directly estimating biomass burning emissions and fuel consumption rates and totals from geostationary satellite fire radiative power (FRP). Remote Sensing of Environment, 206, 45-62, https://doi.org/10.1016/j.rse.2017.12.016.

Nguyen, H.M., & Wooster, M.J. (2020). Advances in the estimation of high Spatio-temporal resolution pan-African top-down biomass burning emissions made using geostationary fire radiative power (FRP) and MAIAC aerosol optical depth (AOD) data. Remote Sensing of Environment, 248, 111971, https://doi.org/10.1016/j.rse.2020.111971.

Nowell, H.K., Holmes, C.D., Robertson, K., Teske, C., & Hiers, J.K. (2018). A New Picture of Fire Extent, Variability, and Drought Interaction in Prescribed Fire Landscapes: Insights From Florida Government Records. Geophysical Research Letters, 45, 7874-7884, https://doi.org/10.1016/10.1029/2018GL078679.

O'Neill, S.M., Diao, M., Raffuse, S., Al-Hamdan, M., Barik, M., Jia, Y., Reid, S., Zou, Y., Tong, D., West, J.J., Wilkins, J., Marsha, A., Freedman, F., Vargo, J., Larkin, N.K., Alvarado, E., & Loesche, P. (2021). A multi-analysis approach for estimating regional health impacts from the 2017 Northern California wildfires. Journal of the Air & Waste Management Association, 71, 791-814, https://doi.org/10.1016/10.1080/10962247.2021.1891994.

Ottmar, R.D. (2014). Wildland fire emissions, carbon, and climate: Modeling fuel consumption. Forest Ecology and Management, 317, 41-50, https://doi.org/10.1016/j.foreco.2013.06.010.

1414 Pan, X., Ichoku, C., Chin, M., Bian, H., Darmenov, A., Colarco, P., Ellison, L., Kucsera, T., da Silva, A., Wang, J.,
1415 Oda, T., & Cui, G. (2020). Six global biomass burning emission datasets: intercomparison and application in
1416 one global aerosol model. Atmos. Chem. Phys., 20, 969-994, https://doi.org/10.1016/10.5194/acp-20-969-2020.
1417 Parker, R.J., Boesch, H., Wooster, M.J., Moore, D.P., Webb, A.J., Gaveau, D., & Murdiyarso, D. (2016).
1418 Atmospheric CH4 and CO2 enhancements and biomass burning emission ratios derived from satellite
1419 observations of the 2015 Indonesian fire plumes. Atmos. Chem. Phys., 16, 10111-10131.
1420 https://doi.org/10.5194/acp-16-10111-2016.
1421 Pereira, G., Freitas, S.R., Moraes, E.C., Ferreira, N.J., Shimabukuro, Y.E., Rao, V.B., & Longo, K.M. (2009).
1422 Estimating trace gas and aerosol emissions over South America: Relationship between fire radiative energy
1423 released and aerosol optical depth observations. Atmospheric Environment, 43, 6388-6397,
1424 https://doi.org/10.1016/j.atmosenv.2009.09.013.
1425 Prichard, S.J., Kennedy, M.C., Andreu, A.G., Eagle, P.C., French, N.H., & Billmire, M. (2019). Next-Generation
1426 Biomass Mapping for Regional Emissions and Carbon Inventories: Incorporating Uncertainty in Wildland Fuel
1427 Characterization. Journal of Geophysical Research: Biogeosciences, 124, 3699-3716, 10.1029/2019jg005083.
1428 Prichard, S.J., O'Neill, S.M., Eagle, P., Andreu, A.G., Drye, B., Dubowy, J., Urbanski, S., & Strand, T.M. (2020).
1429 Wildland fire emission factors in North America: synthesis of existing data, measurement needs and
1430 management applications. International Journal of Wildland Fire, 29, 132-147,
1431 https://doi.org/10.1071/WF19066.
1432 Pyne, S.J., Andrews, P.L., & Laven, R.D. (1996). Introduction to wildland fire. John Wiley and Sons
1433 Ramo, R., Roteta, E., Bistinas, I., van Wees, D., Bastarrika, A., Chuvieco, E., & van der Werf, G.R. (2021). African
1434 burned area and fire carbon emissions are strongly impacted by small fires undetected by coarse resolution
1435 satellite data. Proceedings of the National Academy of Sciences, 118, e2011160118.
1436 https://doi.org/10.1073/pnas.2011160118.
1437 Randerson, J.T., Chen, Y., van der Werf, G.R., Rogers, B.M., & Morton, D.C. (2012). Global burned area and
1438 biomass burning emissions from small fires. Journal of Geophysical Research: Biogeosciences, 117, G04012,
1439 https://doi.org/10.1016/10.1029/2012JG002128.
1440 Reid, J.S., Hyer, E.J., Prins, E.M., Westphal, D.L., Jianglong, Z., Jun, W., Christopher, S.A., Curtis, C.A., Schmidt,
1441 C.C., Eleuterio, D.P., Richardson, K.A., & Hoffman, J.P. (2009). Global Monitoring and Forecasting of

Biomass-Burning Smoke: Description of and Lessons From the Fire Locating and Modeling of Burning Emissions (FLAMBE) Program. Selected Topics in Applied Earth Observations and Remote Sensing, IEEE Journal of, 2, 144-162, https://doi.org/10.1016/10.1109/JSTARS.2009.2027443.

Roberts, G., Wooster, M.J., & Lagoudakis, E. (2009). Annual and diurnal african biomass burning temporal dynamics. Biogeosciences, 6, 849-866, https://doi.org/10.1016/10.5194/bg-6-849-2009.

Roberts, G., Wooster, M.J., Lauret, N., Gastellu-Etchegorry, J.P., Lynham, T., & McRae, D. (2018). Investigating the impact of overlying vegetation canopy structures on fire radiative power (FRP) retrieval through simulation and measurement. Remote Sensing of Environment, 217, 158-171, https://doi.org/10.1016/j.rse.2018.08.015.

Roberts, G., Wooster, M.J., Perry, G.L.W., Drake, N., Rebelo, L.M., & Dipotso, F. (2005). Retrieval of biomass combustion rates and totals from fire radiative power observations: Application to southern Africa using geostationary SEVIRI imagery. Journal of Geophysical Research: Atmospheres, 110, D21111, https://doi.org/10.1016/10.1029/2005JD006018.

Roberts, G., Wooster, M.J., Xu, W., Freeborn, P.H., Morcrette, J.J., Jones, L., Benedetti, A., Jiangping, H., Fisher, D., & Kaiser, J.W. (2015). LSA SAF Meteosat FRP products – Part 2: Evaluation and demonstration for use in the Copernicus Atmosphere Monitoring Service (CAMS). Atmos. Chem. Phys., 15, 13241-13267, https://doi.org/10.1016/10.5194/acp-15-13241-2015.

Roberts, G.J., & Wooster, M.J. (2008). Fire Detection and Fire Characterization Over Africa Using Meteosat SEVIRI. Geoscience and Remote Sensing, IEEE Transactions on, 46, 1200-1218, 10.1109/TGRS.2008.915751.

Roteta, E., Bastarrika, A., Padilla, M., Storm, T., & Chuvieco, E. (2019). Development of a Sentinel-2 burned area algorithm: Generation of a small fire database for sub-Saharan Africa. Remote Sensing of Environment, 222, 1-17, https://doi.org/10.1016/j.rse.2018.12.011.

Roy, D.P., Huang, H., Boschetti, L., Giglio, L., Yan, L., Zhang, H.H., & Li, Z. (2019). Landsat-8 and Sentinel-2 burned area mapping - A combined sensor multi-temporal change detection approach. Remote Sensing of Environment, 231, 111254, https://doi.org/10.1016/j.rse.2019.111254.

Saide, P.E., Peterson, D.A., da Silva, A., Anderson, B., Ziemba, L.D., Diskin, G., Sachse, G., Hair, J., Butler, C., Fenn, M., Jimenez, J.L., Campuzano-Jost, P., Perring, A.E., Schwarz, J.P., Markovic, M.Z., Russell, P., Redemann, J., Shinozuka, Y., Streets, D.G., Yan, F., Dibb, J., Yokelson, R., Toon, O.B., Hyer, E., & Carmichael, G.R. (2015). Revealing important nocturnal and day-to-day variations in fire smoke emissions

1470 through a multiplatform inversion. Geophysical Research Letters, 42, 2015GL063737,
1471 https://doi.org/10.1016/10.1002/2015GL063737.
1472 Schmidt, C.C., Hoffman, J., & Prins, E.M. (2012). GOES-R Advanced Baseline Imager (ABI) Algorithm
1473 Theoretical Basis Document For Fire / Hot Spot Characterization Version 2.5. In (pp. 1-97): NOAA NESDIS
1474 STAR
1475 Schmit, T.J., Griffith, P., Gunshor, M.M., Daniels, J.M., Goodman, S.J., & Lebair, W.J. (2017). A Closer Look at
1476 the ABI on the GOES-R Series. Bulletin of the American Meteorological Society, 98, 681-698,
1477 https://doi.org/10.1016/10.1175/bams-d-15-00230.1.
1478 Schroeder, W., Oliva, P., Giglio, L., & Csiszar, I.A. (2014). The New VIIRS 375 m active fire detection data
1479 product: Algorithm description and initial assessment. Remote Sensing of Environment, 143, 85-96,
1480 https://doi.org/10.1016/10.1016/j.rse.2013.12.008.
1481 Schroeder, Giglio, L., Csiszar, I.A., & Tsidulko, M. (2020). VIIRS Active Fire Algorithm Theoretical Basis
1482 Document, available at:
1483 https://www.star.nesdis.noaa.gov/jpss/documents/ATBD/ATBD_Iband_ActiveFires_v1.0.pdf, last access on
1484 12/1/2021.
1485 Seiler, W., & Crutzen, P. (1980). Estimates of gross and net fluxes of carbon between the biosphere and the
1486 atmosphere from biomass burning. Climatic Change, 2, 207-247, https://doi.org/10.1016/10.1007/BF00137988.
1487 Shindell, D.T., Faluvegi, G., Stevenson, D.S., Krol, M.C., Emmons, L.K., Lamarque, J.-F., Pétron, G., Dentener,
1488 F.J., Ellingsen, K., Schultz, M.G., Wild, O., Amann, M., Atherton, C.S., Bergmann, D.J., Bey, I., Butler, T.,
1489 Cofala, J., Collins, W.J., Derwent, R.G., Doherty, R.M., Drevet, J., Eskes, H.J., Fiore, A.M., Gauss, M.,
1490 Hauglustaine, D.A., Horowitz, L.W., Isaksen, I.S.A., Lawrence, M.G., Montanaro, V., Müller, J.-F., Pitari, G.,
1491 Prather, M.J., Pyle, J.A., Rast, S., Rodriguez, J.M., Sanderson, M.G., Savage, N.H., Strahan, S.E., Sudo, K.,
1492 Szopa, S., Unger, N., van Noije, T.P.C., & Zeng, G. (2006). Multimodel simulations of carbon monoxide:
1493 Comparison with observations and projected near-future changes. Journal of Geophysical Research:
1494 Atmospheres, 111, https://doi.org/10.1016/10.1029/2006jd007100.
1495 Streets, D.G., Canty, T., Carmichael, G.R., de Foy, B., Dickerson, R.R., Duncan, B.N., Edwards, D.P., Haynes, J.A.,
1496 Henze, D.K., Houyoux, M.R., Jacob, D.J., Krotkov, N.A., Lamsal, L.N., Liu, Y., Lu, Z., Martin, R.V., Pfister,
1497 G.G., Pinder, R.W., Salawitch, R.J., & Wecht, K.J. (2013). Emissions estimation from satellite retrievals: A

review of current capability. Atmospheric Environment, 77, 1011-1042, https://doi.org/10.1016/j.atmosenv.2013.05.051.

Swain, D.L. (2021). A Shorter, Sharper Rainy Season Amplifies California Wildfire Risk. Geophysical Research Letters, 48, e2021GL092843, https://doi.org/10.1029/2021GL092843.

Urbanski, S. (2014). Wildland fire emissions, carbon, and climate: Emission factors. Forest Ecology and Management, 317, 51-60, https://doi.org/10.1016/10.1016/j.foreco.2013.05.045.

Urbanski, S.P., Reeves, M.C., Corley, R.E., Silverstein, R.P., & Hao, W.M. (2018). Contiguous United States wildland fire emission estimates during 2003–2015. Earth Syst. Sci. Data, 10, 2241-2274, https://doi.org/10.1016/10.5194/essd-10-2241-2018.

van der Velde, I.R., van der Werf, G.R., Houweling, S., Maasakkers, J.D., Borsdorff, T., Landgraf, J., Tol, P., van Kempen, T.A., van Hees, R., Hoogeveen, R., Veefkind, J.P., & Aben, I. (2021). Vast CO2 release from Australian fires in 2019–2020 constrained by satellite. Nature, 597, 366-369, 10.1038/s41586-021-03712-y.

van der Werf, G.R., Randerson, J.T., Giglio, L., Collatz, G.J., Kasibhatla, P.S., & Arellano Jr, A.F. (2006). Interannual variability in global biomass burning emissions from 1997 to 2004. Atmos. Chem. Phys., 6, 3423-3441, https://doi.org/10.1016/10.5194/acp-6-3423-2006.

van der Werf, G.R., Randerson, J.T., Giglio, L., van Leeuwen, T.T., Chen, Y., Rogers, B.M., Mu, M., van Marle, M.J.E., Morton, D.C., Collatz, G.J., Yokelson, R.J., & Kasibhatla, P.S. (2017). Global fire emissions estimates during 1997–2016. Earth Syst. Sci. Data, 9, 697-720, https://doi.org/10.1016/10.5194/essd-9-697-2017.

van Marle, M.J.E., Kloster, S., Magi, B.I., Marlon, J.R., Daniau, A.L., Field, R.D., Arneth, A., Forrest, M., Hantson, S., Kehrwald, N.M., Knorr, W., Lasslop, G., Li, F., Mangeon, S., Yue, C., Kaiser, J.W., & van der Werf, G.R. (2017). Historic global biomass burning emissions based on merging satellite observations with proxies and fire models (1750-2015). Geosci. Model Dev. 2017, 1-56, https://doi.org/10.1016/10.5194/gmd-2017-32.

van Wees, D., & van der Werf, G.R. (2019). Modelling biomass burning emissions and the effect of spatial resolution: a case study for Africa based on the Global Fire Emissions Database (GFED). Geosci. Model Dev., 12, 4681-4703, https://doi.org/10.1016/10.5194/gmd-12-4681-2019.

Veefkind, J.P., Aben, I., McMullan, K., Förster, H., de Vries, J., Otter, G., Claas, J., Eskes, H.J., de Haan, J.F., Kleipool, Q., van Weele, M., Hasekamp, O., Hoogeveen, R., Landgraf, J., Snel, R., Tol, P., Ingmann, P., Voors, R., Kruizinga, B., Vink, R., Visser, H., & Levelt, P.F. (2012). TROPOMI on the ESA Sentinel-5 Precursor: A

GMES mission for global observations of the atmospheric composition for climate, air quality and ozone layer applications. Remote Sensing of Environment, 120, 70-83, https://doi.org/10.1016/j.rse.2011.09.027.

Veraverbeke, S., & Hook, S.J. (2013). Evaluating spectral indices and spectral mixture analysis for assessing fire severity, combustion completeness and carbon emissions. International Journal of Wildland Fire, 22, 707-720, https://doi.org/10.1016/10.1071/WF12168.

Vermote, E., Ellicott, E., Dubovik, O., Lapyonok, T., Chin, M., Giglio, L., & Roberts, G.J. (2009). An approach to estimate global biomass burning emissions of organic and black carbon from MODIS fire radiative power. Journal of Geophysical Research: Atmospheres, 114, D18205, https://doi.org/10.1016/10.1029/2008JD011188.

Vetrita, Y., Cochrane, M.A., Suwarsono, Priyatna, M., Sukowati, K.A.D., & Khomarudin, M.R. (2021). Evaluating accuracy of four MODIS-derived burned area products for tropical peatland and non-peatland fires. Environmental Research Letters, 16, 035015, https://doi.org/10.1016/10.1088/1748-9326/abd3d1.

Wang, J., Bhattacharjee, P.S., Tallapragada, V., Lu, C.H., Kondragunta, S., da Silva, A., Zhang, X., Chen, S.P., Wei, S.W., Darmenov, A.S., McQueen, J., Lee, P., Koner, P., & Harris, A. (2018). The implementation of NEMS GFS Aerosol Component (NGAC) Version 2.0 for global multispecies forecasting at NOAA/NCEP – Part 1: Model descriptions. Geosci. Model Dev., 11, 2315-2332, https://doi.org/10.1016/10.5194/gmd-11-2315-2018.

Weise, D.R., & Wright, C.S. (2014). Wildland fire emissions, carbon and climate: Characterizing wildland fuels. Forest Ecology and Management, 317, 26-40, https://doi.org/10.1016/10.1016/j.foreco.2013.02.037.

Wiedinmyer, C., Akagi, S.K., Yokelson, R.J., Emmons, L.K., Al-Saadi, J.A., Orlando, J.J., & Soja, A.J. (2011). The Fire INventory from NCAR (FINN): a high resolution global model to estimate the emissions from open burning. Geosci. Model Dev., 4, 625-641, https://doi.org/10.1016/10.5194/gmd-4-625-2011.

Wiggins, E.B., Soja, A.J., Gargulinski, E., Halliday, H.S., Pierce, R.B., Schmidt, C.C., Nowak, J.B., DiGangi, J.P., Diskin, G.S., Katich, J.M., Perring, A.E., Schwarz, J.P., Anderson, B.E., Chen, G., Crosbie, E.C., Jordan, C., Robinson, C.E., Sanchez, K.J., Shingler, T.J., Shook, M., Thornhill, K.L., Winstead, E.L., Ziemba, L.D., & Moore, R.H. (2020). High Temporal Resolution Satellite Observations of Fire Radiative Power Reveal Link Between Fire Behavior and Aerosol and Gas Emissions. Geophysical Research Letters, 47, e2020GL090707, https://doi.org/10.1029/2020GL090707.

Williams, A.P., Abatzoglou, J.T., Gershunov, A., Guzman-Morales, J., Bishop, D.A., Balch, J.K., & Lettenmaier, D.P. (2019). Observed Impacts of Anthropogenic Climate Change on Wildfire in California. Earth's Future, 7, 892-910, https://doi.org/10.1016/10.1029/2019ef001210.

Wolfe, R.E., Lin, G., Nishihama, M., Tewari, K.P., Tilton, J.C., & Isaacman, A.R. (2013). Suomi NPP VIIRS prelaunch and on-orbit geometric calibration and characterization. Journal of Geophysical Research: Atmospheres, 118, 2013JD020508, https://doi.org/10.1016/10.1002/jgrd.50873.

Wooster, M.J. (2002). Small-scale experimental testing of fire radiative energy for quantifying mass combusted in natural vegetation fires. Geophysical Research Letters, 29, 2027, https://doi.org/10.1016/10.1029/2002GL015487.

Wooster, M.J., Gaveau, D.L.A., Salim, M.A., Zhang, T., Xu, W., Green, D.C., Huijnen, V., Murdiyarso, D., Gunawan, D., Borchard, N., Schirrmann, M., Main, B., & Sepriando, A. (2018). New Tropical Peatland Gas and Particulate Emissions Factors Indicate 2015 Indonesian Fires Released Far More Particulate Matter (but Less Methane) than Current Inventories Imply. Remote Sensing, 10, 495, https://doi.org/10.3390/rs10040495.

Wooster, M.J., Roberts, G., Perry, G.L.W., & Kaufman, Y.J. (2005). Retrieval of biomass combustion rates and totals from fire radiative power observations: FRP derivation and calibration relationships between biomass consumption and fire radiative energy release. Journal of Geophysical Research-Atmospheres, 110, D24311, https://doi.org/10.1016/10.1029/2005jd006318.

Wooster, M.J., Roberts, G.J., Giglio, L., Roy, D., Freeborn, P., Boschetti, L., Justice, C., Ichoku, C., Schroeder, W., Davies, D., Smith, A., Setzer, A., Csiszar, I., Strydom, T., Frost, P., Zhang, T., Xu, W., de Jong, M., Johnston, J., Ellison, L., Vadrevu, K., McCarty, J., Tanpipat, V., Schmidt, C., & San-Miguel, J. (2021). Satellite remote sensing of active fires: History and current status, applications and future requirements. Remote Sensing of Environment, 267, 112694, https://doi.org/10.1016/j.rse.2021.112694.

Xu, W., Wooster, M.J., He, J., & Zhang, T. (2021a). Improvements in high-temporal resolution active fire detection and FRP retrieval over the Americas using GOES-16 ABI with the geostationary Fire Thermal Anomaly (FTA) algorithm. Science of Remote Sensing, 3, 100016, https://doi.org/10.1016/j.srs.2021.100016.

Xu, W., Wooster, M.J., Polehampton, E., Yemelyanova, R., & Zhang, T. (2021b). Sentinel-3 active fire detection and FRP product performance - Impact of scan angle and SLSTR middle infrared channel selection. Remote Sensing of Environment, 261, 112460. https://doi.org/10.1016/j.rse.2021.112460.

Xu, W., Wooster, M.J., Kaneko, T., He, J., Zhang, T., & Fisher, D. (2017). Major advances in geostationary fire radiative power (FRP) retrieval over Asia and Australia stemming from use of Himarawi-8 AHI. Remote Sensing of Environment, 193, 138-149, https://doi.org/10.1016/j.rse.2017.02.024.

Ye, X., Arab, P., Ahmadov, R., James, E., Grell, G.A., Pierce, B., Kumar, A., Makar, P., Chen, J., Davignon, D., Carmichael, G.R., Ferrada, G., McQueen, J., Huang, J., Kumar, R., Emmons, L., Herron-Thorpe, F.L., Parrington, M., Engelen, R., Peuch, V.H., da Silva, A., Soja, A., Gargulinski, E., Wiggins, E., Hair, J.W., Fenn, M., Shingler, T., Kondragunta, S., Lyapustin, A., Wang, Y., Holben, B., Giles, D.M., & Saide, P.E. (2021). Evaluation and intercomparison of wildfire smoke forecasts from multiple modeling systems for the 2019 Williams Flats fire. Atmos. Chem. Phys., 21, 14427-14469, https://doi.org/10.5194/acp-21-14427-2021.

Yokelson, R.J., Burling, I.R., Gilman, J.B., Warneke, C., Stockwell, C.E., de Gouw, J., Akagi, S.K., Urbanski, S.P., Veres, P., Roberts, J.M., Kuster, W.C., Reardon, J., Griffith, D.W.T., Johnson, T.J., Hosseini, S., Miller, J.W., Cocker Iii, D.R., Jung, H., & Weise, D.R. (2013). Coupling field and laboratory measurements to estimate the emission factors of identified and unidentified trace gases for prescribed fires. Atmos. Chem. Phys., 13, 89-116, https://doi.org/10.5194/acp-13-89-2013.

Yokelson, R.J., Crounse, J.D., DeCarlo, P.F., Karl, T., Urbanski, S., Atlas, E., Campos, T., Shinozuka, Y., Kapustin, V., Clarke, A.D., Weinheimer, A., Knapp, D.J., Montzka, D.D., Holloway, J., Weibring, P., Flocke, F., Zheng, W., Toohey, D., Wennberg, P.O., Wiedinmyer, C., Mauldin, L., Fried, A., Richter, D., Walega, J., Jimenez, J.L., Adachi, K., Buseck, P.R., Hall, S.R., & Shetter, R. (2009). Emissions from biomass burning in the Yucatan. Atmos. Chem. Phys., 9, 5785-5812, https://doi.org/10.5194/acp-9-5785-2009.

Yokelson, R.J., Karl, T., Artaxo, P., Blake, D.R., Christian, T.J., Griffith, D.W.T., Guenther, A., & Hao, W.M. (2007). The Tropical Forest and Fire Emissions Experiment: overview and airborne fire emission factor measurements. Atmos. Chem. Phys., 7, 5175-5196, https://doi.org/10.5194/acp-7-5175-2007.

Zhang, F., Wang, J., Ichoku, C., Hyer, E.J., Yang, Z., Ge, C., Su, S., Zhang, X., Kondragunta, S., & Kaiser, J.W. (2014a). Sensitivity of mesoscale modeling of smoke direct radiative effect to the emission inventory: a case study in northern sub-Saharan African region. Environmental Research Letters, 9, 075002, https://doi.org/10.1088/1748-9326/9/7/075002.

Zhang, T., de Jong, M.C., Wooster, M.J., Xu, W., & Wang, L. (2020). Trends in eastern China agricultural fire emissions derived from a combination of geostationary (Himawari) and polar (VIIRS) orbiter fire radiative power products. Atmos. Chem. Phys., 20, 10687-10705, https://doi.org/10.5194/acp-20-10687-2020.

Zhang, X., Kondragunta, S., Da Silva, A., Lu, S., Ding, H., Li, F., & Zhu, Y. (2019). The Blended Global Biomass Burning Emissions Product from MODIS and VIIRS Observations (GBBEPx) Version 3.1. In: NOAA/NESDIS/STAR

Zhang, X., Kondragunta, S., Ram, J., Schmidt, C., & Huang, H.-C. (2012). Near-real-time global biomass burning emissions product from geostationary satellite constellation. Journal of Geophysical Research-Atmospheres, 117, D14201, https://doi.org/10.1029/2012jd017459.

Zhang, X., Kondragunta, S., & Roy, D.P. (2014b). Interannual variation in biomass burning and fire seasonality derived from geostationary satellite data across the contiguous United States from 1995 to 2011. Journal of Geophysical Research: Biogeosciences, 119, 2013JG002518, https://doi.org/10.1002/2013JG002518.

Zhang, X., Kondragunta, S., Schmidt, C., & Kogan, F. (2008). Near real time monitoring of biomass burning particulate emissions (PM2.5) across contiguous United States using multiple satellite instruments. Atmospheric Environment, 42, 6959-6972, https://doi.org/10.1016/j.atmosenv.2008.04.060.

Zheng, Y., Liu, J., Jian, H., Fan, X., & Yan, F. (2021). Fire Diurnal Cycle Derived from a Combination of the Himawari-8 and VIIRS Satellites to Improve Fire Emission Assessments in Southeast Australia. Remote Sensing, 13, 2852, https://doi.org/10.3390/rs13152852.

List of Figure Captions

Figure 1. Land cover and ecoregion maps across the CONUS.

Figure 2. Flowchart of generating hourly 3 km emissions using ABI and VIIRS FRP. Note that the ABI and VIIRS fire detections are preprocessed data after removing false alarms based on a temporal filter and persistent anomaly flags (c.f. Sections 2.1 and 2.2).

Figure 3. Comparison of GOES-16 and GOES-17 ABI FRP in four fires in 2020. Among these fires, GOES-17 VZA changed slightly between 46° and 50° while GOES-16 VZA varied largely from 53° to 64°, as shown in the VZA legend (for GOES-16). G17 and G16 in legend are abbreviations for GOES-17 and GOES-16, respectively. Each sample represents total FRP in a fire observed by both satellites at the same time.

Figure 4. Comparison of contemporaneous ABI and VIIRS FRP in fire clusters. (a) Daytime and (b) nighttime. Each sample represent FRP observed by GOES-16 ABI and Suomi-NPP or NOAA-20 VIIRS contemporaneously (within ±2.5 min).

Figure 5. The land cover-ecoregion-specific FRP diurnal climatologies derived from GOES-16 and GOES-17 ABI FRP observations. The left column (a-e) shows the normalized diurnal FRP in five land cover types: forest, shrubland, savanna, grassland, and cropland. Each normalized diurnal curve was obtained by calculating the ratio of the diurnal mean FRP values to the peak-

time mean FRP value. The right column (f-j) shows the associated peak-time mean FRP in the five land cover types.

Figure 6. An example of fire sample selection. (a-d) show the process of choosing one fire event based on TROPOMI CO observations and Suomi NPP VIIRS and GOES-16 ABI true-color images and active fire detections. The fire occurred near Austin in South Texas (the United States) on 10 December 2020. (a) Suomi NPP VIIRS true-color image with VIIRS and ABI fire detections observed at 19:36 UTC and 19:41 UTC, respectively. (b) TROPOMI CO column dry air mixing ratio (unit: parts per billion by volume or ppbv in short) observed at around 19:41 UTC, with smoke plume in warm colors. (c) Delineated smoke CO and background CO overlain on the Suomi NPP VIIRS true-color image. The upwind and all-directions backgrounds are delineated using white and pink polygons. (d) Time series of GOES-16 ABI true-color images shows the evolution of the smoke plume during 17:21 – 19:46 UTC.

Figure 7. Annual total dry matter (a) and $PM_{2.5}$ emissions (b) in 3 km grids from April 2020 – March 2021.

Figure 8. Land cover-specific diurnal patterns of $PM_{2.5}$ emissions. $PM_{2.5}$ diurnal patterns in (a) five land cover types across the whole CONUS, and (b) Forest across the west and east CONUS.

Figure 9. Hourly total $PM_{2.5}$ emission from three California largest wildfires in 2020. (a) The August Complex Fire during the week from 4 – 10 September 2020, (b) the Creek Fire during

1679 the week from 5-11 September 2020, and (c) the North Complex Fire during the week from 11-
1680 17 September.

1681

1682 **Figure 10.** Monthly total mass of $PM_{2.5}$ emissions in five land cover types during one year from
1683 April 2020 to March 2021. Note that forest $PM_{2.5}$ uses the second y-axis on the right.

1684

1685 **Figure 11**. Comparison of CO emissions in the selected fires. (a) Distribution of the selected 27
1686 fires overlain on the land cover map (as in Figure 1a). The inset shows a fire example. Red, black,
1687 and purple polygons delineate TROPOMI CO observations in smoke plume and background. (b)
1688 The TROPOMI CO column mixing ratio of smoke plume and upwind background in the selected
1689 fires (colored by longitude), with their mean values denoted by circles and squares, respectively.
1690 Error bars show the 20th and 80th percentile CO column mixing ratios. (c) Comparison of
1691 RAVE and TROPOMI CO mass in the selected fires.

1692

1693 **Figure 12.** $PM_{2.5}$ emissions in eight inventories. (a) Annual total $PM_{2.5}$ and (b) monthly total
1694 $PM_{2.5}$. Y-axis in (b) uses a logarithmic scale. Note that FINN2.4 $PM_{2.5}$ emissions only account
1695 for 9 months from April – December 2020 because it was not available for 2021 when the
1696 analysis was performed.

1697

1698 **Figure 13**. PM2.5 maps of California's largest August Complex Fire in 2020 from six emissions
1699 datasets. (a) 3 km RAVE1.0, (b) 0.1 degree GFAS1.2, (c) 0.1° FEER1.0, (d) 0.1° GBBEPx4.0, (e)
1700 0.25° GFED4s, and (f) 0.25° × 0.3125° QFED2.5. The black line is the buffered Landsat (30m)-
1701 based fire perimeter outward by 3km.

1702

1703 **Figure 14.** Comparison of the TROPOMI CO estimates based on the upwind and all-direction

1704 backgrounds over the selected 27 fires.